

**Material Characterization of Additive Manufactured Metals Using a Line-Focus  
Transducer System**

by

**Ruixin Feng**

Bachelor of Science, University of Pittsburgh, 2019

Submitted to the Graduate Faculty of the  
Swanson School of Engineering in partial fulfillment  
of the requirements for the degree of  
Master of Science in Mechanical Engineering

University of Pittsburgh

2021

UNIVERSITY OF PITTSBURGH  
SWANSON SCHOOL OF ENGINEERING

This thesis was presented

by

**Ruixin Feng**

It was defended on

April 6, 2021

and approved by

Qing-Ming Wang, Ph.D., Professor

Department of Mechanical Engineering and Materials Science

Patrick Smolinski, Ph.D., Associate Professor

Department of Mechanical Engineering and Materials Science

William Slaughter, Ph.D., Associate Professor

Department of Mechanical Engineering and Materials Science

Thesis Advisor: Qing-Ming Wang, Ph.D., Professor

Department of Mechanical Engineering and Materials Science

Copyright © by Ruixin Feng

2021

# **Material Characterization of Additive Manufactured Metals Using a Line-Focus Transducer System**

Ruixin Feng., M.S.

University of Pittsburgh, 2021

Additive manufacturing has thrived over the past decade due to its prominent potential of fast prototyping and complex components fabrication. Unlike conventional manufacturing that subtracts the desired products from the raw materials, 3D printing builds components upon layers, which may result in some degrees of uncertain shifts in terms of the material properties. While enhancing in-situ monitoring provides improving quality assurance during the process, reliable nondestructive methods are on-demand to provide the feedback of end products' elastic properties.

A line-focus transducer system that utilizes ultrasound for material characterization is presented. The main hardware is a large aperture lens-less line-focus transducer with a theoretical central frequency of  $10\text{MHz}$ , while a time-resolved method is adopted to avoid any mechanical scanning. This testing method is based on the propagation of surface and bulk acoustic waves and their relationship with mediums' elastic properties. The system is first validated by measuring conventionally produced metal bars and then applied to Stainless Steel 316L samples that are manufactured from Direct Metal Laser Sintering 3D printer. Sufficient signal processing and data analysis are conducted to predict samples' elastic properties' actual values, indicating a good match with the information on the official datasheet.

This research aims to 1) introduce the fundamental of the piezoelectric effect, nondestructive testing methods, and additive manufacturing methods, 2) establish a solid

understanding of the relationship between acoustic wave propagation and the stiffness constants.

3) build up a reliable line-focus transducer system with neat experiment and analysis procedure,

4) conclude the result and future expectations.

## Table of Contents

Preface.....	xii
<b>1.0 Introduction and Background .....</b>	<b>1</b>
<b>1.1 Piezoelectric Effect .....</b>	<b>2</b>
1.1.1 The history of piezoelectricity .....	2
1.1.2 Linear theory of piezoelectricity .....	2
1.1.3 Piezoelectric coefficient $d$ .....	4
1.1.4 Piezoelectrical materials .....	5
<b>1.2 Nondestructive Testing Method .....</b>	<b>7</b>
<b>1.3 Additive Manufacturing Method .....</b>	<b>8</b>
1.3.1 3D-printing methods.....	8
1.3.2 Additive Manufacturing Research Laboratory.....	9
1.3.3 Laser powder-bed fusion process .....	10
<b>2.0 Theoretic Foundation .....</b>	<b>12</b>
<b>2.1 Acoustic Wave.....</b>	<b>12</b>
2.1.1 Bulk wave propagation and elastic constant .....	14
2.1.2 Rayleigh wave propagation .....	18
<b>2.2 The Development of Line-Focus Transducer.....</b>	<b>22</b>
<b>2.3 Green's Function Prediction .....</b>	<b>25</b>
<b>3.0 Experimental Design and System Configuration.....</b>	<b>28</b>
<b>3.1 Measurement Principles .....</b>	<b>28</b>
3.1.1 Snell's law and critical angle .....	28

<b>3.1.2 Detailed measurement principle .....</b>	<b>30</b>
<b>3.2 Transducer Fabrication .....</b>	<b>33</b>
<b>3.3 System Configuration.....</b>	<b>35</b>
<b>3.4 System Calibration .....</b>	<b>38</b>
<b>4.0 Experiment Result and Analysis.....</b>	<b>42</b>
<b>4.1 Additive Manufactured Metals .....</b>	<b>42</b>
<b>4.2 Wave Diagrams and Numerical Result .....</b>	<b>44</b>
<b>4.3 Summary .....</b>	<b>56</b>
<b>5.0 Future Work.....</b>	<b>58</b>
<b>Appendix A MATLAB Program .....</b>	<b>60</b>
<b>Bibliography .....</b>	<b>64</b>

## List of Tables

<b>Table 1. Modes of vibration for plate shape piezoelectric material .....</b>	<b>6</b>
<b>Table 2. Comparisons between the piezoelectric properties of some common piezoelectric materials.....</b>	<b>7</b>
<b>Table 3. Wave velocity and elastic constants of common metal alloys .....</b>	<b>41</b>
<b>Table 4. Material Composition of EOS Stainless Steel 316L .....</b>	<b>43</b>
<b>Table 5. Calculated result of sample 1 .....</b>	<b>53</b>
<b>Table 6. Calculated result of sample 2 and sample 3.....</b>	<b>54</b>
<b>Table 7. A predicted range of actual elastic properties based on testing results .....</b>	<b>56</b>

## List of Figures

<b>Figure 1. Schematic of polyvinylidene fluoride (PVDF) film.....</b>	<b>6</b>
<b>Figure 2. schematic of the process of recoating and spreading a new layer of powder over the previously fused layers of the part .....</b>	<b>11</b>
<b>Figure 3. Propagation of longitudinal wave .....</b>	<b>12</b>
<b>Figure 4. Propagation of shear wave.....</b>	<b>13</b>
<b>Figure 5. Propagation of Rayleigh wave .....</b>	<b>13</b>
<b>Figure 6. Propagation of love wave .....</b>	<b>13</b>
<b>Figure 7. The direction of Stress Components.....</b>	<b>14</b>
<b>Figure 8. Rayleigh wave propagation (a) coordinate system and (b) elliptic orbit.....</b>	<b>19</b>
<b>Figure 9. (a) the horizontal and vertical amplitude of particle motions in coordinate (b) elliptical polarization of particle motion in a Rayleigh wave in a homogeneous half space .....</b>	<b>22</b>
<b>Figure 10. Periodic maxim and minima of <math>V(z)</math> curve .....</b>	<b>24</b>
<b>Figure 11. 2D and 3D Green's function prediction and experimental waveform.....</b>	<b>27</b>
<b>Figure 12. Reflection and refraction of acoustic wave at interface .....</b>	<b>29</b>
<b>Figure 13. A schematic of critical angles for different acoustic waves .....</b>	<b>29</b>
<b>Figure 14. The wave propagation of line-focus transducer when (a) sample surface is at the focal plane (b) the sample is defocused with a distance <math>z</math>.....</b>	<b>30</b>
<b>Figure 15. a) Radiation of Rayleigh wave from a surface element into an adjacent fluid with acoustic wavelength <math>\lambda</math> (b) Energy balance for a surface element during time <math>dt</math> due to radiation or leaking of the Rayleigh wave into an adjacent fluid.....</b>	<b>31</b>

Figure 16. (a) PVDF film and (b) its frequency response.....	34
Figure 17. The assembly of large aperture lens-less line-focus transducer .....	34
Figure 18. The machined aluminum tube as transducer case. ....	35
Figure 19. A schematic of the measurement system .....	36
Figure 20. The fixation of the transducer to the motor stage .....	36
Figure 21. The output signal $V(t)$ curve when (a) sample surface is at the focal plane (b) the sample is defocused .....	38
Figure 22. Experimental waveform from stainless steel 420 sample.....	39
Figure 23. $z(t)$ plot of stainless steel 420.....	40
Figure 24. 3D printed SS 316L samples with marker.....	43
Figure 25. Depiction of using engineering notebook sheet to align the sample and transducer .....	43
Figure 26. $V(z,t)$ curves of sample 1 with a step size of 0.2, the 1 <sup>th</sup> track .....	45
Figure 27. $Z(t)$ plot of sample 1 with a step size of 0.2, the 1 <sup>th</sup> track.....	45
Figure 28. $V(z,t)$ curves of sample 1 with a step size of 0.2, the 2 <sup>th</sup> track .....	46
Figure 29. $Z(t)$ plot of sample 1 with a step size of 0.2, the 2 <sup>th</sup> track.....	46
Figure 30. $V(z,t)$ curves of sample 1 with a step size of 0.25, the 1 <sup>th</sup> track .....	47
Figure 31. $Z(t)$ plot of sample 1 with a step size of 0.25, the 1 <sup>th</sup> track.....	47
Figure 32. $V(z,t)$ curves of sample 1 with a step size of 0.25, the 2 <sup>th</sup> track.....	48
Figure 33. $Z(t)$ plot of sample 1 with a step size of 0.25, the 2 <sup>th</sup> track.....	48
Figure 34. $V(z,t)$ curves of sample 2 with a step size of 0.2 .....	49
Figure 35. $Z(t)$ plot of sample 2 with a step size of 0.2.....	49
Figure 36. $V(z,t)$ curves of sample 2 with a step size of 0.25 .....	50

<b>Figure 37. Z(t) plot of sample 2 with a step size of 0.25.....</b>	<b>50</b>
<b>Figure 38. V(z,t) curves of sample 3 with a step size of 0.2 .....</b>	<b>51</b>
<b>Figure 39. Z(t) plot of sample 3 with a step size of 0.2.....</b>	<b>51</b>
<b>Figure 40. V(z,t) curves of sample 3 with a step size of 0.25 .....</b>	<b>52</b>
<b>Figure 41. Z(t) plot of sample 3 with with a step size of 0.25 .....</b>	<b>52</b>
<b>Figure 42. The average Young's modulus with standard deviation error bar .....</b>	<b>55</b>
<b>Figure 43. The average shear modulus with standard deviation error bar .....</b>	<b>55</b>
<b>Figure 44. The average Poisson's ratio with standard deviation error bar.....</b>	<b>56</b>
<b>Figure 45. A 3D printed cylinder metal bar .....</b>	<b>58</b>
<b>Figure 46. Schematic of line-focus transducer measurement principle with a cylinder sample</b> <b>.....</b>	<b>59</b>
<b>Figure 47. (a) measured waveforms of 3D-time domain; (b) normalized waveforms of time-</b> <b>domain.....</b>	<b>59</b>

## Preface

Completing my master's study during this special time is hard but memorable. I would like to present my sincere gratitude to all the kind people that have supported me throughout my research study. First of all, I would like to thank my advisor Prof. Qing-Ming Wang for all his guidance and support. He always encourages me to be more confident and committed. I want to express sincere appreciation to my committee members, Dr. Patrick Smolinski and Dr. William Slaughter, for the comments and suggestions.

Secondly, I appreciate the great help from the Ph.D. students in our research group: Saleh Awad Alghamdi and Zihao Zhong. Special thanks to my senior fellows, Qiuyan Li, Huining Wang, and Menghan Jiang, for taking the time to answer my questions. Also, thank all my research group members. There is no way I could finish my thesis without these people's assistance and company.

In addition, my gratitude to my parents for their selfless love.

## **1.0 Introduction and Background**

With the gradual maturity of 3D printing, this novel technology brings digital flexibility and efficiency to manufacturing, and its fields of application have expanded fast and tremendously. Although traditional quality and property tests can be used for 3D printed parts, problems are exposed, especially when they are in complicated shapes and not mass-produced. Therefore, different nondestructive testing methods are come into being in such areas. This study presents a line-focus transducer system that belongs to ultrasound testing to measure the elastic properties.

In the following sections of this chapter, backgrounds related to the development of this transducer system are briefly introduced, including the piezoelectric effect, various nondestructive testing methods, and additive manufacturing.

In chapter 2, theoretical foundations that establish the relationship between wave propagation and elastic properties are provided in detail. The evolution of this line-focus transducer and its waveform prediction are also described.

In chapter 4, the hardware configuration, measurement principle, and testing procedure of this system are explained and validated by applying to standard metal alloys.

The result is listed and analyzed in chapter 5, while chapter 6 delivers the conclusion and draws the future work.

## 1.1 Piezoelectric Effect

### 1.1.1 The history of piezoelectricity

Piezoelectricity indicates the phenomenon that charges accumulating on the surface of some materials when mechanical stress is applied [1]. The direct piezoelectric effect was first discovered by the Curie brothers in 1880. By examining six crystal species with known pyroelectricity properties, they observed that compression or tension of asymmetric crystals could generate electric polarization. The induced voltage was proportional to the applied mechanical stress and with a reverse sign when the direction of stress is changed. Conversely, the inverse piezoelectric effect, which is characterized as geometric strain proportionally generating in response to an applied electric field, was discovered by Gabriel Lippmann in 1881 and later confirmed by Curies [2]. Modern exploration of piezoelectrical technology really speeded up in the past few decades, along with novel materials discovery and market stimulation. Over the years, innovative piezoelectricity applications have gradually penetrated various industry fields, including automation, information, telecommunication, medical instrument, etc.

### 1.1.2 Linear theory of piezoelectricity

This section briefly provides the three-dimensional formulation of linear piezoelectricity in a Cartesian coordinate system to further interpret the piezoelectric effect. There are several essential indexes when evaluating piezoelectric materials: the strain component  $S_{ij}$ , the stress component  $T_{ij}$ , the electric field intensity  $E_i$ , and electric displacement  $D_i$ . When the external electric field is applied, the last two vectors are related as:

$$D_i = \epsilon_0 E_i + P_i \quad (1-1)$$

where  $P_i$  is the polarization vector, and  $\epsilon_0$  is the permittivity of free space and given by  $\epsilon_0 = 8.854 \times 10^{-12} F/m$ . The conservation of energy equation for the linear piezoelectric continuum can be represented as:

$$\dot{U} = T_{ij} \dot{S}_{ij} + E_i \dot{D}_i \quad (1-2)$$

where  $U$  is the stored energy density for piezoelectric material. The electric enthalpy density  $H$  is defined as:

$$H = U - E_i D_i = \frac{1}{2} c_{ijkl}^E S_{ij} S_{kl} - e_{kij} E_k S_{ij} - \frac{1}{2} \epsilon_{ij}^S E_i E_j \quad (1-3)$$

where  $c_{ijkl}^E$  is elastic constant, while  $e_{kij}$  and  $\epsilon_{ij}^S$  are piezoelectric and dielectric constants, respectively. By taking partial derivatives, one form of piezoelectric constitutive equations can be found as:

$$T_{ij} = c_{ijkl}^E S_{kl} - e_{kij} E_k \quad (1-4)$$

$$D_i = e_{ikl} S_{kl} + \epsilon_{ik}^S E_k \quad (1-5)$$

which is called  $e$ -form (stress-charge form) of linear piezoelectricity. Other alternate forms of constitutive equations include  $d$ -form (strain-charge form):

$$S_{ij} = s_{ijkl}^E T_{kl} + d_{kij} E_k \quad (1-6)$$

$$D_i = d_{ikl} T_{kl} + \epsilon_{ik}^T E_k \quad (1-7)$$

$g$ -form:

$$S_{ij} = s_{ijkl}^D T_{kl} + g_{kij} D_k \quad (1-8)$$

$$E_i = -g_{ikl} T_{kl} + \beta_{ik}^T D_k \quad (1-9)$$

and  $h$ -form:

$$T_{ij} = c_{ijkl}^D S_{kl} - h_{hij} D_k \quad (1-10)$$

$$E_i = -h_{ikl}S_{kl} + \beta_{ik}^S D_k \quad (1-11)$$

where  $d_{kij}$  is the piezoelectric strain constants,  $g_{kij}$  represents piezoelectric voltage constant,  $h_{ikl}$  is the piezoelectric charge constant, and  $\beta_{ik}^S$  indicates electric impermeability for constant stress and strain. In the above forms of equations, the first equations in every set describe the directed piezoelectric effect, while the second ones explain the inverse piezoelectric effect.

### 1.1.3 Piezoelectric coefficient $d$

If consider the elastic and piezoelectric tensors in matrix form, the piezoelectric strain constant  $d$  relates the polarization  $P$  and the stress  $X$  as:

$$\begin{pmatrix} P_1 \\ P_2 \\ P_3 \end{pmatrix} = \begin{pmatrix} d_{11} & d_{12} & d_{13} & d_{14} & d_{15} & d_{16} \\ d_{21} & d_{22} & d_{23} & d_{24} & d_{25} & d_{26} \\ d_{31} & d_{32} & d_{33} & d_{34} & d_{35} & d_{36} \end{pmatrix} \begin{pmatrix} X_1 \\ X_2 \\ X_3 \\ X_4 \\ X_5 \\ X_6 \end{pmatrix} \quad (1-12)$$

conversely, when an external electric field  $E$  is conducted, the induced stress  $X$  in 3-dimensions expression can be indicated as:

$$\begin{pmatrix} X_1 \\ X_2 \\ X_3 \\ X_4 \\ X_5 \\ X_6 \end{pmatrix} = \begin{pmatrix} e_{11} & e_{12} & e_{13} \\ e_{21} & e_{22} & e_{23} \\ e_{31} & e_{32} & e_{33} \\ e_{41} & e_{42} & e_{43} \\ e_{51} & e_{52} & e_{53} \\ e_{61} & e_{62} & e_{63} \end{pmatrix} \begin{pmatrix} E_1 \\ E_2 \\ E_3 \end{pmatrix} \quad (1-13)$$

the electromechanical coupling factor  $k$  can be interpreted as:

$$k^2 = \frac{\text{Stored Mechanical Energy}}{\text{Input Electrical Energy}} = \frac{\text{Input Electrical Energy}}{\text{Stored Mechanical Energy}}$$

this value is related to the conversion rate between electrical energy and mechanical energy. The mechanical quality factor  $Q$  describes the sharpness of the electromechanical resonance frequency.

The acoustic impedance  $Z$  estimates the acoustic energy transfer efficiency from one material to another. In a solid material,  $Z$  can be denoted as:

$$Z = \sqrt{\rho c} \quad (1-14)$$

where  $\rho$  is the density, and  $c$  is the elastic constant.

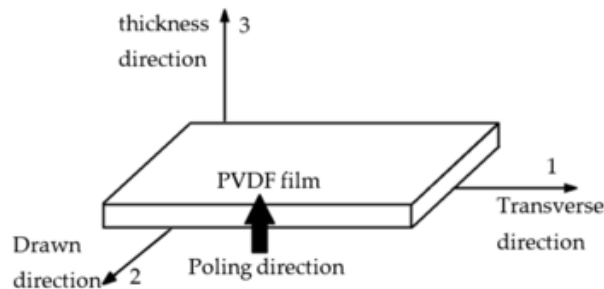
#### 1.1.4 Piezoelectrical materials

Generally, piezoelectric effects are found in two main categories of non-conductive materials: crystals and ceramics. The piezoelectrical element used in this method is PVDF (polyvinylidene difluoride) film, which has been the dominant material among piezoelectric polymers. Its piezoelectricity was discovered by H. Kawai at Kureha in 1969 [3]. In this category of materials, the polymer chain contains strong molecular dipoles, contributing to the piezoelectricity when their density has been changed by applied mechanical stimulus [3]. Overall, piezoelectric polymers are relatively lighter and have soft elasticity [4], leading to higher flexibility. The acoustic impedance of PVDF is comparable to that of water and other liquids, while its piezoelectricity's thermal stability is limited to under 100 °C [3]. Furthermore, PVDF sheets have a low mechanical quality factor  $Q$  that results in a broad resonance bandwidth.

PVDF and its ferroelectric polymers are semicrystalline structures and belong to the orthorhombic  $mm2$  symmetry group. Thus, the number of independent components of matrix  $d$  can be reduced to 5 [5]. In this case, the piezoelectric strain constant  $d$  matrix becomes:

$$d = \begin{vmatrix} 0 & 0 & 0 & 0 & d_{15} & 0 \\ 0 & 0 & 0 & d_{24} & 0 & 0 \\ d_{31} & d_{32} & d_{33} & 0 & 0 & 0 \end{vmatrix} \quad (1-15)$$

As mentioned before, the poling direction is usually taken as direction 3, which, in this case, is the thickness direction of the PVDF film, as shown in Figure 1. The PVDF film works as thickness mode, which means the generated vibration responding to the applied voltage is in the thickness direction, as shown in Table 1. Furthermore, a comparison between the piezoelectric properties of some common piezoelectric materials is shown in Table 2. Compared to common ceramic materials such as PZT, PVDF has a moderate and negative  $d_{33}$  coefficient (around  $-20 \text{ pC/N}$ ) [1].



[6]

**Figure 1.** Schematic of polyvinylidene fluoride (PVDF) film

**Table 1.** Modes of vibration for plate shape piezoelectric material

Axis	Material Shape	Polarization Direction	Applied Field/Voltage Output	Model of Vibration/Displacement
				<p>length or transverse (l or w)</p> <p>thickness (h)</p>

[7]

**Table 2.** Comparisons between the piezoelectric properties of some common piezoelectric materials

Comparison of piezoelectric materials					
Property	Units	PVDF Film	PZT	Barium Titanate	EMFI PP Film
		at 28 microns)			(at 70 microns)
Density	$10^3 \text{ kg m}^{-3}$	1.78	7.5	5.7	330
Relative Permittivity	$\epsilon/\epsilon_0$	12	1200	1700	1.2
d31 Piezoelectric Constant	$10^{-12} \text{ C/N}$	23	110	78	2
g31 Voltage Constant	$10^{-3} \text{ Vm/N}$	216	10	5	
k31 Electromechanical Constant	% at 1kHz	12	30	21	
P Pyroelectric Constant	$\text{Cm}^{-2}\text{K}$	30		025 to 0.45	
Acoustic Impedance	$10^6 \text{ kgm}^{-1}\text{s}^{-1}$	2.7	30	30	
Youngs Modulus	$\text{Nm}^{-2}$	2-4			<1
Surface Resistivity	$\text{ohm/sq}$	0.1			<2
Dynamic Range	$\text{Pa}$	$1-5 \times 10^9$			$<1 \times 10^6$
Temperature Range	C	-40 to 100 (130 with some copolymers)			-40 to 50
Glass Transition Temperature	K	223			278

[8]

## 1.2 Nondestructive Testing Method

The measurement of materials' structures and properties is a fundamental process to provide a scientific understanding of engineering materials being used. Most conventional characterization techniques are destructive testing that is carried out to the specimen's failure, such as tensile test. Although destructive testing is suitable and convenient for mass-produced objects, it is not economical when there are only one or a few items [9, 3]. Not to mention some of those testing methods require specific shape and size samples, and the data processing is time-consuming [10]. Therefore, different Nondestructive Testing (NDT) methods, which enable to characterize materials, detect flaws, and assure products' performance without damaging the specimen, have been developed to fulfill the industry's need and provide engineers with more comprehensive information [11].

Commonly used NDT methods including visual and optical testing (VT), radiography (RT), magnetic testing (MT), electromagnetic testing, acoustic emission testing (AE), and ultrasound testing (UT) [11]. The testing method that is demonstrated in this research belongs to

the UT category. Generally, ultrasound testing uses high-frequency sound energy to examine material properties and structural integrity [11]. The piezoelectrical transducer converts the generated high voltage electrical pulse into an acoustic wave signal that is later transformed back into an electrical signal after propagating through the material and being reflected. The electronic equipment can display the signal instantaneously and collect the data for further interpretation. The inspection principle and experiment configuration will be elaborated on in the following parts.

### **1.3 Additive Manufacturing Method**

#### **1.3.1 3D-printing methods**

Additive manufacturing (AM), also described as 3D-printing, refers to manufacturing technologies that build physical parts layer-by-layer based on computer-aided design (CAD) files. Compared to conventional manufacturing methods, AM has a good potential for rapid prototyping, automatic manufacturing, and producing complex-shaped products, making it a promising manufacturing method. Ever since Hull invented the first AM method -- stereolithography (SLA) and created the first 3D-printed object in the late 1980s [12], AM technologies have drawn much attention and flourished. Over the past forty years, researchers have developed various types of AM methods, which have been characterized into seven large groups based on the building process and the materials being used. Material extrusion, vat polymerization, material jetting, and sheet lamination are more used in polymer manufacturing. On the other hand, powder bed fusion, directed energy deposition, powder bed binder jetting are common metal additive manufacturing

methods [12]. Different AM technologies have been adopted widely in the aerospace, automotive, architecture, and biomedical industry.

Besides the freedom of complexity, 3D printing has two more superior features in terms of metal fabrication: the potential of allowing printed parts to be topologically optimized and produced from high-strength materials that are hard to process using traditional methods. However, due to the unique production process, the mechanical properties of products made from 3D-printing somehow differ from those made by traditional manufacturing methods with the same materials. Moreover, the lack of reproducibility and the quality issues resulting from porosity level and distributions are the two main drawbacks that prevent 3D-printing methodology from being more widely adopted. Therefore, to further establish AM as core manufacturing methods, reliable methods are needed to conduct materials characterization as well as quality control and monitoring for AM products.

### **1.3.2 Additive Manufacturing Research Laboratory**

The Additive Manufacturing Research Laboratory (AMRL) of the University of Pittsburgh was founded in 2016 and is dedicated to provides Pitt faculty and research partners with a range of AM technologies and customary services. There are several different 3D-printers available in the lab: an EOS M290, which is a Direct Metal Laser Sintering (DMLS) powder bed machine; an Optomec LENS 450 that uses a direct metal deposition process; an ExOne M-Flex and an ExOne Lab, while both of them use a powder bed binder jet process; a Stratasys Objet 260 Connex 3D polyjet printer. Research related to additive manufacturing, such as topology optimization and residual stress mitigation, is conducted in the lab. Besides, quality control based on different printing settings is investigated to prevent porosity of the end-use product.

The microstructure and mechanical properties of AM components are always of interest due to the lack of a reliable theoretical prediction model based on the wide range of input printing settings. In terms of DMSL printed metal, the process parameters are usually optimized to maximize density to reduce porosity, while in-situ monitoring is conducted to ensure the components' integrity. On the other hand, regarding mechanical properties, an in-time and reliable NDE system that can provide such feedback would benefit researchers with a more comprehensive understanding of the printed items when the ultimate goal is to optimize the products' quality and performance. The line-focus ultrasound testing system is presented here for material characterization. The system is validated by testing standard manufactured metals as a perspective NDT method that utilizes the Rayleigh wave to obtain the elastic properties.

### **1.3.3 Laser powder-bed fusion process**

In this research, the tested AM metals from AMRL are produced by the EOS M290 DMLS machine. The DMLS is a Laser Powder Bed Fusion technology, which, specifically, is an AM process that uses a laser beam as the heat source to selectively sinter materials in powder form to build 3D object layer-by-layer based on model data. As shown in Figure 2, during the process, a laser beam is generated to pass through a system of lenses and reflected by an X-Y scanning mirror onto the upper layer of the building part that is supported by the build platform. The X-Y scanning mirror is used to control the laser beam movement while material powder consolidates along the path. After completing the melting of one layer, the build piston moves downward, and the recoating blade pushes and spreads a new layer of powder from the powder dispenser over the build area. The whole process will repeat until the 3D printing is finished. Since the unfused

material powder stays in the build tank, there are no unsupported overhangs during the process and thus no need for a support structure.

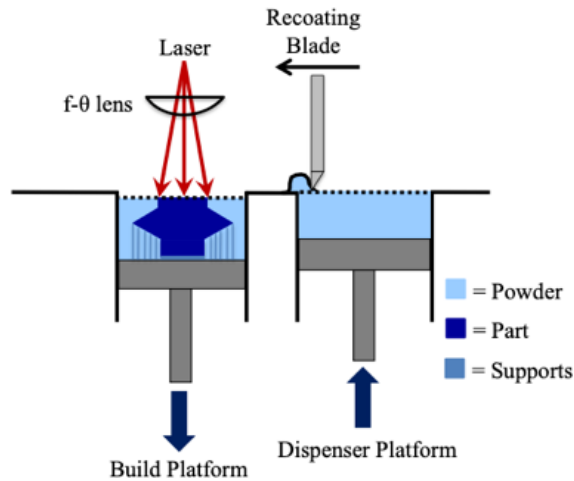


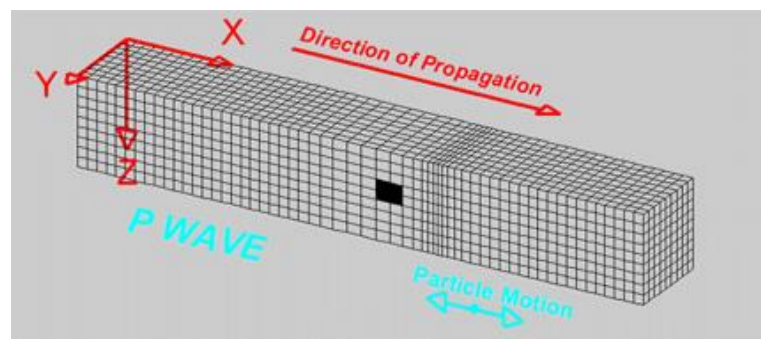
**Figure 2.** schematic of the process of recoating and spreading a new layer of powder over the previously fused layers of the part

The EOS M290 machine utilizes a 400-watt fiber laser with a scanning speed of up to 7.0m/s, and the focus diameter is around 100  $\mu\text{m}$ . Such high energy and excellent resolution enable an adequate production of metal components with tailored complex shapes while ensuring homogeneous part properties. This machine also includes comprehensive in-situ monitoring systems that allow real-time quality assurance. Besides, there is a wide range of choices of materials that can be used to fulfill customers' requirements, such as EOS Aluminium AlSi10Mg, EOS NickelAlloy IN625, EOS Titanium Ti64, and EOS Stainless Steel 316L. Since this research aims to validate the feasibility of using the line-focus transducer system to quickly provide trustable material properties information of AM products, samples manufactured from such a sophisticated 3D printer would exhibit the dependable intrinsic property that contributes to the system's further upgrade.

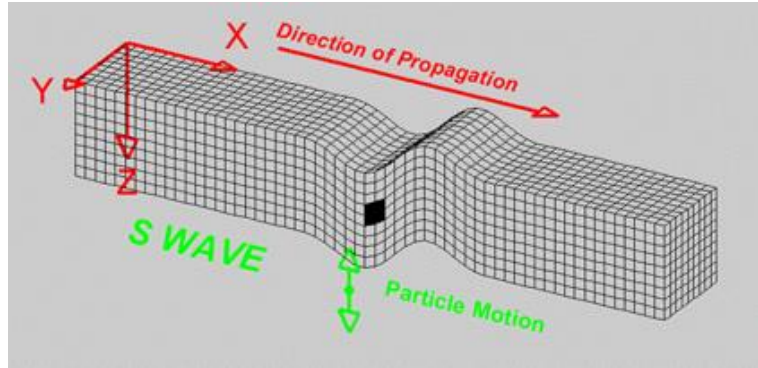
## 2.0 Theoretic Foundation

### 2.1 Acoustic Wave

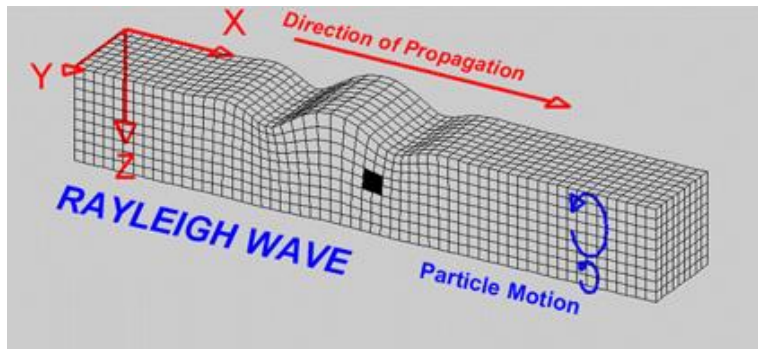
Acoustic waves are a form of energy transmission in a medium in response to an oscillation of pressure. In a gas or a fluid, sound only travels by compressing and decompressing molecules in the direction of propagation. However, since solids can support vibration in other directions, there are several types of sound waves in solids that can be generated. Longitudinal wave, also known as P wave or primary wave in seismology, refers to the waveform in that particles move in the same direction as the wave moving. Transverse wave, which is also called a shear wave, S wave, or secondary wave, transmits in a direction that is perpendicular to that of the particle moving. Both longitudinal wave and transverse wave are bulk acoustic waves (BAW) that travel inside a solid. In addition to BAW, other forms of acoustic waves can be incited under special conditions. For example, Rayleigh wave is a type of surface acoustic wave (SAW) and propagates on the stress-free surface of a semi-infinite solid [13]; Lamb wave and Love wave are plate waves that are similar to SAW except they can only be generated in thin solids a few wavelengths thick [11]. Figures 3, 4, 5, and 6 depict how the above-mentioned wave propagates, respectively.



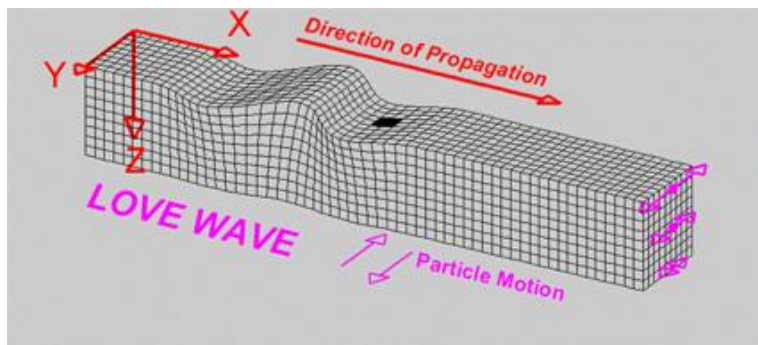
**Figure 3.** Propagation of the longitudinal wave



**Figure 4.** Propagation of the shear wave



**Figure 5.** Propagation of Rayleigh wave



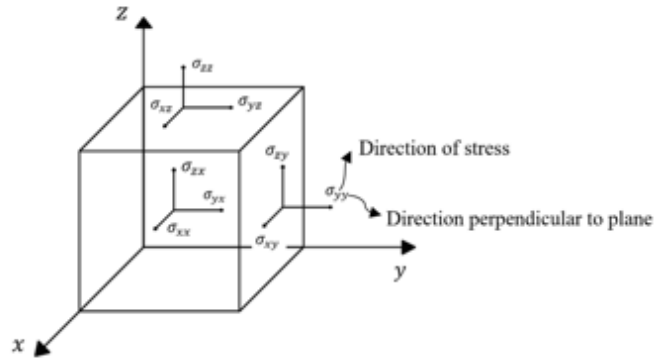
**Figure 6.** Propagation of love wave

Image © 2000-2006 Lawrence Braille, used with permission.

### 2.1.1 Bulk wave propagation and elastic constant

When an acoustic wave propagates within an elastic solid, deformation happens locally due to the strain results from the stress. The displacement of each point from its original position varies continuously throughout the medium and has components corresponding to stress in different directions, as shown in Figure 7. The stress components are identified as  $\sigma_{ij}$ . The local displacement can be represented as a vector  $u(x, y, z, t)$  [14]; thus, the strain matrix  $\epsilon_{kl}$  can be derived and interpreted as:

$$\epsilon_{kl} = \frac{1}{2} \left( \frac{\partial u_k}{\partial x_l} + \frac{\partial u_l}{\partial x_k} \right), k, l = x, y, z \quad (2-1)$$



**Figure 7.** Direction of Stress Components

For elastic materials under small deformations, the strain is proportional to the applied stress. This principle can be defined using generalized Hooke's law as a succinct statement of the linear relationship among all the components of the stress and strain tensor:

$$\sigma_{ij} = C_{ijkl} \epsilon_{kl} \quad (2-2)$$

where the  $C_{ijkl}$  is called the elastic stiffness constant, and it is a 4<sup>th</sup> rank tensor with an original total  $3^4=81$  elements. Since both stress and strain tensors are symmetric, the number of indices can be reduced and expressed as:

$$\sigma_I = C_{IJ}\epsilon_J \quad (2-3)$$

where I and J range from 1 to 6. The stiffness matrix  $C_{IJ}$  is also symmetric so, a total 21 elements are required at most to characterize the material.

In the case of an isotropic medium, the elastic properties are identical in all directions at every point; thus, the stiffness matrix can be simplified as:

$$C_{IJ} = \begin{vmatrix} C_{11} & C_{12} & C_{12} & 0 & 0 & 0 \\ C_{12} & C_{11} & C_{12} & 0 & 0 & 0 \\ C_{12} & C_{12} & C_{11} & 0 & 0 & 0 \\ 0 & 0 & 0 & C_{44} & 0 & 0 \\ 0 & 0 & 0 & 0 & C_{44} & 0 \\ 0 & 0 & 0 & 0 & 0 & C_{44} \end{vmatrix} \quad (2-4)$$

With a relationship  $C_{44} = (C_{11} - C_{12})/2$ , there are only two independent variables. By introducing the Lamè constants  $\lambda$  and  $\mu$  [15], the stress and strain link of isotropic material can be written in matrix form as:

$$\begin{vmatrix} \sigma_1 \\ \sigma_2 \\ \sigma_3 \\ \sigma_4 \\ \sigma_5 \\ \sigma_6 \end{vmatrix} = \begin{vmatrix} \lambda + 2\mu & \lambda & \lambda & 0 & 0 & 0 \\ \lambda & \lambda + 2\mu & \lambda & 0 & 0 & 0 \\ \lambda & \lambda & \lambda + 2\mu & 0 & 0 & 0 \\ 0 & 0 & 0 & \mu & 0 & 0 \\ 0 & 0 & 0 & 0 & \mu & 0 \\ 0 & 0 & 0 & 0 & 0 & \mu \end{vmatrix} \begin{vmatrix} \epsilon_1 \\ \epsilon_2 \\ \epsilon_3 \\ \epsilon_4 \\ \epsilon_5 \\ \epsilon_6 \end{vmatrix} \quad (2-5)$$

In addition, the Lamè constants are related to Young's modulus  $E$  and Poisson ratio  $\nu$  in the following expressions:

$$\lambda = \frac{E\nu}{(1 + \nu)(1 - 2\nu)} \quad (2-6)$$

$$\mu = G = \frac{E}{2(1 + \nu)} \quad (2-7)$$

Based on previous derivation of stress and strain relationship as well as the elastic property tensor, the equation of motion for elements in isotropic material can be obtained by analyzing the force exerted and applying Newton's law,  $F = m\ddot{u}$ . Take x-direction, for example, the total acting force:

$$\begin{aligned} F_1 &= \Delta T_{11}\Delta y\Delta z + \Delta T_{12}\Delta x\Delta z + \Delta T_{13}\Delta x\Delta y \\ &= m\ddot{u}_1 = \rho\Delta x\Delta y\Delta z \frac{\partial^2 u_1}{\partial t^2} \end{aligned} \quad (2-8)$$

By further simplifying, a general expression of the equation of motion to all three coordinates can be generated:

$$\sum_{j=1}^3 \frac{\partial T_{ij}}{\partial x_j} = \rho \frac{\partial^2 u_i}{\partial t^2} \quad (2-9)$$

where  $T$  is an alternative representation of stress, same as  $\sigma$ . Similarly, the strain matrix will be denoted as  $S_{kl}$  instead of  $\epsilon_{kl}$  in the subsequent derivation process. Because of the symmetry of the strain matrix,  $S_{kl} = \frac{\partial u_k}{\partial x_l}$ , the equation of motion can be further interpreted as:

$$\sum_{j=1}^3 \frac{\partial T_{ij}}{\partial x_j} = \sum_{j,k,l=1}^3 C_{ijkl} \frac{\partial^2 u_k}{\partial x_j \partial x_l} = \rho \frac{\partial^2 u_i}{\partial t^2} \quad (2-10)$$

Generally, the solution to the above equation consists of three forms of the wave with orthogonal polarization and transmit in the same direction with different velocities. A quasi-longitudinal wave has a principal polarization lying along the propagation direction, while the other two are quasi-shear waves with perpendicular polarizations to the propagation direction. To derive the set of wave equations for isotropic material, assume the plane waves propagate along the x-direction,

then the partial derivatives with respect to  $y$  and  $z$  are zero. Applying the stiffness matrix  $C_{IJ}$  can result in the following partial differential equations:

$$\rho \frac{\partial^2 u_1}{\partial t^2} = C_{11} \frac{\partial^2 u_1}{\partial x^2} \quad (2-11)$$

$$\rho \frac{\partial^2 u_2}{\partial t^2} = C_{44} \frac{\partial^2 u_2}{\partial x^2} \quad (2-12)$$

$$\rho \frac{\partial^2 u_3}{\partial t^2} = C_{44} \frac{\partial^2 u_3}{\partial x^2} \quad (2-13)$$

A solution to each of these equations is:

$$u_i(x, t) = u_{i0} e^{j(\omega t - kx)} \quad (2-14)$$

In this case,  $u_1$  represents a compressional wave that propagates along the  $x$  axis, and  $u_2, u_3$  represents the two shear waves that propagate along  $x$  axis. By substituting the general form of solution into the above equations of wave motion, the dispersion relation for the compressional wave becomes:

$$\rho \omega^2 = C_{11} k^2 \quad (2-15)$$

With the relation wave velocity  $v = \omega/k$ , the velocities of longitudinal wave  $v_L$  and shear wave  $v_S$  can be calculated and expressed as:

$$v_L = \sqrt{C_{11}/\rho} = \sqrt{\frac{\lambda + 2\mu}{\rho}} \quad (2-16)$$

$$v_S = \sqrt{C_{44}/\rho} = \sqrt{\frac{\mu}{\rho}} \quad (2-17)$$

By combining and solving the above equations of elastic properties and wave velocities, below elastic constants can be found:

$$E = \rho v_s^2 \frac{3v_L^2 - 4v_s^2}{v_L^2 - v_s^2} \quad (2-18)$$

$$G = \rho v_s^2 \quad (2-19)$$

$$v = \frac{2v_s^2 - 4v_L^2}{2(v_s^2 - v_L^2)} \quad (2-20)$$

### 2.1.2 Rayleigh wave propagation

Rayleigh wave is a unique waveform that propagates along the surface of a solid due to the stress-free characteristic of the boundary [14]. In 1885, Lord Rayleigh first brought up the significant impact of surface waves in an earthquake and later discovered this particular mode of wave propagation in 1887 [16]. When the Rayleigh wave is transmitting, its velocity differs from bulk acoustic waves, and the surface particles present an elliptical orbit movement results from the coupled longitudinal and shear motion.

To better analyze the Rayleigh wave propagation, consider a coordinate system is shown in Figure 8 (a) in which a wave polarized in the sagittal (x-z) plane and move along the x direction. There are only displacement and velocity components of particle movement in the x and z directions, which means no transvers components in the y direction:  $v_y = 0$  [14]. Thus, the elliptic orbit is shown in Figure 8 (b) only appears in x-z plane.

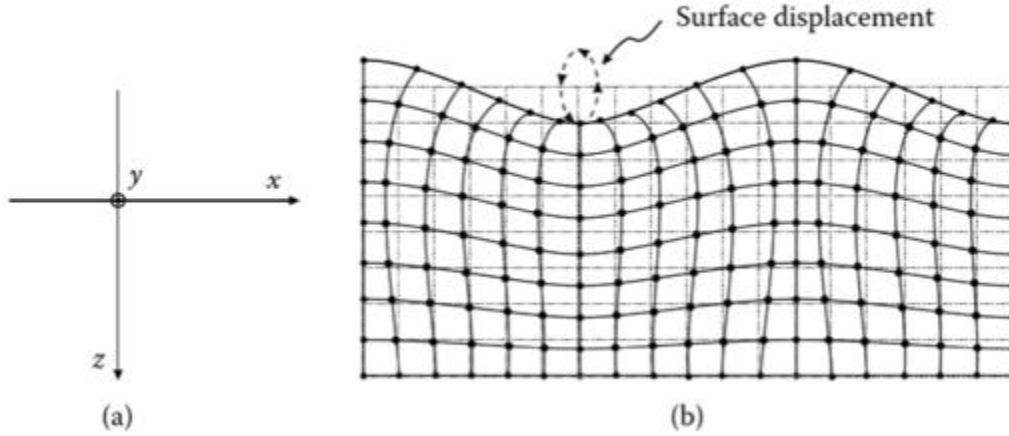


**Figure 8.** Rayleigh wave propagation (a) coordinate system and (b) elliptic orbit

Referring to bulk acoustic waves (BAW), the displacement vector  $u$  can be written as the gradient of a scalar and the curl of a vector as:

$$\vec{u} = \vec{\nabla}\phi + \vec{\nabla} \times \vec{\psi} \quad (2-21)$$

where  $\phi$  are scalar potentials for the longitudinal wave component, and  $\vec{\psi}$  are vector potentials for the transverse wave component. The corresponding wave equations are:

$$\frac{\partial^2 \phi}{\partial x^2} + \frac{\partial^2 \phi}{\partial z^2} + k_L^2 \phi = 0 \quad (2-22)$$

$$\frac{\partial^2 \psi}{\partial x^2} + \frac{\partial^2 \psi}{\partial z^2} + k_S^2 \psi = 0 \quad (2-23)$$

where  $k_L$  and  $k_S$  are the usual bulk wavenumbers as:

$$k_L = \sqrt{\frac{\rho}{\lambda + 2\mu}} \quad (2-24)$$

$$k_S = \sqrt{\frac{\mu}{\rho}} \quad (2-25)$$

assuming that the wavenumber of Rayleigh wave is  $\beta = k_R$ , and the governing equations for the surface acoustic waves could be predicted as:

$$\phi = F(z)\exp j(\omega t - \beta x) \quad (2-26)$$

$$\psi = G(z)\exp j(\omega t - \beta x) \quad (2-27)$$

by combining wave potential equations and governing equations, the following new relations correlate to the two new functions  $F(z)$  and  $G(z)$  can be derived:

$$\frac{d^2 F}{dz^2} - (\beta^2 - k_L^2) F = 0 \quad (2-28)$$

$$\frac{d^2 G}{dz^2} - (\beta^2 - k_S^2) G = 0 \quad (2-29)$$

the relationship between the quantities of these three wavenumbers is:

$$k_L^2 < k_S^2 < \beta^2 \quad (2-30)$$

by solving the function  $F(z)$  and  $G(z)$ , the governing equation can be written as:

$$\phi = A \exp(-\gamma_L z) \exp j(\omega t - \beta x) \quad (2-31)$$

$$\psi = B \exp(-\gamma_S z) \exp j(\omega t - \beta x) \quad (2-32)$$

where,

$$\gamma_L^2 = \beta^2 - k_L^2 \quad (2-33)$$

$$\gamma_S^2 = \beta^2 - k_S^2 \quad (2-34)$$

$A$  and  $B$  are two arbitrary constants. The goal of Rayleigh wave analysis is to solve its velocity, which relates to the propagation constant (the wavenumber)  $\beta$  and has nothing to do with the amplitude. Consider the stress-free criteria for surface wave propagation on a semi-infinite solid; the boundary conditions are the tangential and normal stresses are zero at  $z = 0$  while the displacements are unknown ( $T_{xz} = T_{zz} = 0$ ). An equation for  $\beta$  can be obtained as:

$$4\beta^2 \gamma_L \gamma_S - (\beta^2 + \gamma_S^2)^2 = 0 \quad (2-35)$$

this equation can be written in below conventional form:

$$\eta^6 - 8\eta^4 + 8(3 - 2\xi^2)\eta^2 - 16(1 - \xi^2) = 0 \quad (2-36)$$

where,

$$\eta = \frac{k_S}{\beta} = \frac{v_R}{v_S} \quad (2-37)$$

$$\xi = \frac{k_L}{k_S} = \frac{v_S}{v_L} \quad (2-38)$$

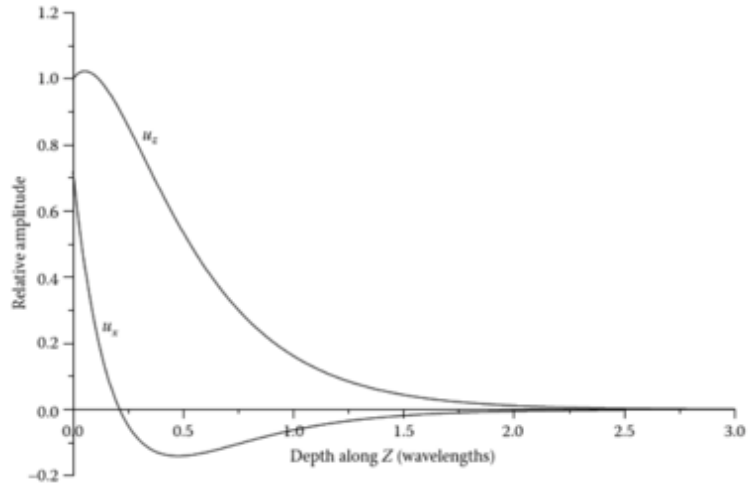
an approximate relationship between Rayleigh wave velocity  $v_R$ , shear wave velocity  $v_S$  and Poisson's ratio  $\nu$  has been proposed by Viktorov [17] as:

$$\eta_R = \frac{0.87 + 1.12\nu}{1 + \nu} \quad (2-39)$$

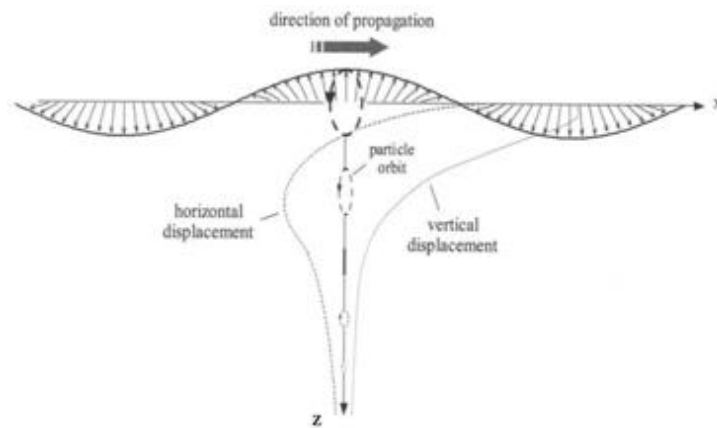
since the range of Poisson's ratio is  $0 < \nu < 0.5$ , the Rayleigh wave velocity criteria set through shear wave should be around  $0.87v_S < v_R < 0.96v_S$ . For isotropic material, a relationship between the speed of longitudinal wave, shear wave, and Rayleigh wave is also proposed by Viktorov [18] as:

$$v_R = v_S \frac{0.718 - \left(\frac{v_S}{v_L}\right)^2}{0.75 - \left(\frac{v_S}{v_L}\right)^2} \quad (2-40)$$

as mentioned before, the Rayleigh wave particle motion is elliptical because of the  $\frac{\pi}{2}$  phase difference between the horizontal and vertical components' displacement field. Also, since the Rayleigh wave was generated due to the stress-free property of the surface, the amplitude of particle motion attenuates exponentially as the depth increases. These relationships can be reflected more intuitively in the coordinate system as Figure 9 (a) and (b), which show how the amplitude in  $z$  (vertical displacement) and  $x$  (horizontal displacement) direction change along with the increase of depth.



(a)



[17]

(b)

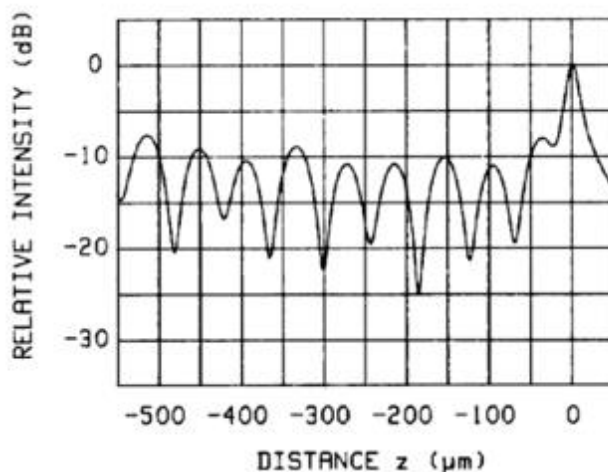
**Figure 9.** (a) the horizontal and vertical amplitude of partial motions in coordinate (b) elliptical polarization of particle motion in a Rayleigh wave in a homogeneous half space

## 2.2 The Development of Line-Focus Transducer

The development of the current line-focus transducer and the relevant testing method can be traced back to the 1970s. In 1973, Lemons and Quate first proposed a mechanically scanned

acoustic microscope with 10- $\mu\text{m}$  resolution. The main part of their system is a pair of single surface acoustic lenses arranged as mirror images, and the object is placed along the symmetry plane. The piezoelectrical elements are attached to the far end of both acoustic lens rods, while one acts as a transmitter, and the opposite one is for receiving the signal after penetrating the specimen [19]. They emphasized that compared to optical waves, the acoustic wave's scattering is solely determined by the change of the medium's elastic properties, making acoustic microscopy a promising instrument that allows researchers to observe details of low optical contrast structures. Since then, lots of research has been conducted worldwide to either optimize the existing hardware of this system or expand its fields of applications [20].

The application of acoustic microscope can be divided into two directions: acoustic imaging measurement and quantitative measurement. One of the quantitative measurement applications is elastic property characterization. In 1979, Weglein reported that the amplitude of the reflected wave  $V$  in acoustic microscope exhibits periodicity along with the change of the distance  $z$  between the sample surface and the focal point of the lens. In other words, the  $V(z)$  curves show repeated maxima and minima as Figure 10. This phenomenon is due to the interference between the axial wave and the Rayleigh wave. Later, Parmon and Bertoni developed the mathematical relationship between the periodic interval  $z$  and the Rayleigh wave velocity  $v_R$  [21]. Thus, the velocity and attenuation of leaky surface waves can be estimated based on the interval between neighboring minima and the minima's depth, respectively [22].



[20]

**Figure 10.** Periodic maxim and minima of  $V(z)$  curve

Ever since its establishment, the  $V(z)$  curves had been fully employed to interpret the contrast in acoustic images quantitatively. However, the original microscope system that used a spherical lens cannot detect anisotropic material's acoustic properties since the radiation from the transducer is point-focused, which means the measurement result is a mean value from all directions. To eliminate this limitation, Kushibiki and Chubachi developed a line-focus beam acoustic microscope with an operation frequency of around 200MHz and published the final version in 1985 [20]. They used a cylindrical concave sapphire lens in their system and fully presented its principle and capability of measuring various materials' properties based on the  $V(z)$  curve. On the other side, in 1982, Liang and his colleagues developed a 50 MHz acoustic microscope system. They demonstrated a new technique that separated longitudinal and Rayleigh wave shortly in the time domain by using a 3-cycle tone burst to measure Rayleigh wave velocity perturbation more conveniently and precisely [23]. Subsequently, Yamanaka was inspired by Liang and proposed a time-resolved defocusing method that could measure the absolute surface wave velocity and attenuation without  $V(z)$  curve, avoiding any mechanical scanning.

It is worth noticing, the acoustic microscopy system generally combined small aperture lenses and high-frequency tone burst to provide a high spatial resolution, benefiting the microscope imaging but also resulting in a higher cost. In 1995, enlightened by predecessors, Xiang created a large aperture lens-less line-focus PVDF transducer that had a focal length of 25.4 mm and an aperture of 28.2 mm with a half angle of  $34^\circ$  [24]. To generate Rayleigh wave more efficiently, Xiang chose lens-less to achieve a low f-number (ratio of focal length to aperture). The rectangular PVDF film, which has an effective electrode size of  $30\text{ mm} \times 12\text{ mm}$  and a thickness of  $28\ \mu\text{m}$ , is selected as the piezoelectrical element for two reasons: its flexibility made it easy to be conformed to the curve, and its low acoustic impedance matches both the backing material and coupling liquid. The transducer's central frequency is 10 MHz, enabling the transducer to be compatible with conventional pulser/receiver. Dr. Xiang adopted the time-resolved method and precisely measured the longitudinal wave speed, leaky surface wave speed, and sample thickness.

The line-focus transducer manufactured and used in this research mainly refers to Dr. Xiang's work. The time-revolved method was chosen to avoid any mechanical scanning that requires an expensive and sophisticated driven system. In comparison to Dr. Xiang's design, the active rectangular PVDF film in our line-focus transducer has a dimension of  $60\text{ mm} \times 12.5\text{ mm}$  and a thickness of  $30\ \mu\text{m}$ . The focal length is 35 mm, and the half aperture angle is  $50^\circ$ . The details of transducer fabrication and time-resolved measurement process will be provided later.

### **2.3 Green's Function Prediction**

A quantitative prediction of line-focus transducer's behavior can be carried out by applying a dynamic Green's function derived by N. N. Hsu in 1992 [25]. The three-dimensional green's

function, shown as below equation, can model the wave behavior at a horizontal liquid/solid interface with both source and detector in the liquid.

$$g(X, T) = \frac{1}{2\pi^2} \int_0^X \text{Real} \left[ \frac{\frac{R_a - R_b}{R_a + R_b}}{\sqrt{q^2 - 1} \left[ -s + \frac{1}{\sqrt{q^2 - 1}} \right] \sqrt{X^2 - s^2}} \right] ds \quad (2-41)$$

where  $X = d/h$  and  $T = tV_w/h$  are normalized variables,  $d$  is the horizontal distance between the point source and receiver,  $h$  is the sum of the source and receiver heights from the interface.  $V_w$  is the sound velocity in the liquid, and  $t$  is the time. Moreover, other dependent variables are:

$$q = \frac{sT}{T^2 - 1} + i \frac{\sqrt{T^2 - 1 - s^2}}{T^2 - 1} \quad (2-42)$$

$$R_a = 4\sqrt{(\alpha^2 q^2 - 1)(\beta^2 q^2 - 1)} + (\beta^2 q^2 - 2)^2 \quad (2-43)$$

$$R_b = \sigma \beta^4 q^4 \frac{\sqrt{\alpha^2 q^2 - 1}}{\sqrt{q^2 - 1}} \quad (2-44)$$

$$\alpha = \frac{V_w}{V_L}, \quad \beta = \frac{V_w}{V_S}, \quad \sigma = \frac{\rho_w}{\rho_s} \quad (2-45)$$

where  $\rho_w$  and  $\rho_s$  are the density of liquid and solid, respectively, and  $V_S$  and  $V_L$  are shear and longitudinal wave speeds in the solid. The symbol  $s$  in above formula is the integrand has at most three singularities, and integration can be carried out along the real axis when below locations are applied [24]:

$$S_w = \sqrt{T^2 - 1}, \quad (2-46)$$

$$S_s = T / \beta - \sqrt{(1/\beta)^2 - 1}, \quad (2-47)$$

$$S_l = T / \alpha - \sqrt{(1/\alpha)^2 - 1}, \quad (2-48)$$

According to Dr. Xiang's work, the transducer response function can be written as [26]:

$$H(t, z) = r^2 \int_{-\alpha}^{\alpha} \int_{-\alpha}^{\alpha} g(X, T) d\theta_0 d\theta \quad (2-49)$$

where  $r$  is the focal length,  $\alpha$  is the half-angle of the transducer,  $\theta_0$  and  $\theta$  are integration variables representing the angle of source and receiver with the symmetry plane, and,

$$d = r|\sin\theta_0 - \sin\theta| \quad (2-50)$$

$$h = r|\cos\theta_0 + \cos\theta| + 2z \quad (2-51)$$

$$\alpha = \sin^{-1}(a/r) \quad (2-52)$$

After integration calculation, the wave behavior can be predicted as below in figure 11, in the case of the defocusing distance  $z=5.5\text{mm}$ . The 2D Green's function is a simplification of 3-D Green's function by assuming both the generator and receiver are infinite in the width direction. It is obvious to see that 3D Green's function is more concordance with the experimental waveform.

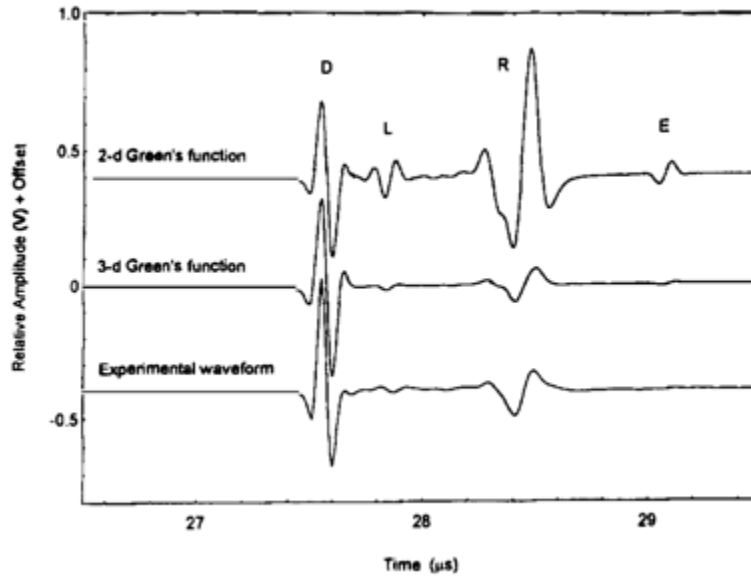


**Figure 11.** 2D and 3D Green's function prediction and experimental waveform

## 3.0 Experimental Design and System Configuration

### 3.1 Measurement Principles

#### 3.1.1 Snell's law and critical angle

When an ultrasound wave crosses the boundary of two mediums at an oblique angle, both reflection and refraction happen due to the material's property differences. In this experiment, the phenomenon mentioned above took place at the interface between distilled water and the test sample. In addition, since there are various types of particle movements within an isotropic solid, the incident wave would generate one longitudinal wave and one transverse wave. To further interpret the principle of measurement, it is necessary to mention Snell's law, which indicates that the ratio of sines of the angle of incidence and refraction equals the ratio of wave velocity in the corresponding medium. As shown in Figure 12, in which  $L_1$  represents the longitudinal wave that transmit in water and reaches the sample surface at an incident angle  $\theta_1$ . Part of the wave energy is reflected back as  $L_1'$ , while  $L_2$  and  $S_2$  represent the refracted longitudinal wave and the refracted shear wave respectively. According to Snell's law, the below equation could be used to relate the waves' velocities and their angles in Figure 12:

$$\frac{\sin\theta_1}{v_{L_1}} = \frac{\sin\theta_L}{v_{L_2}} = \frac{\sin\theta_s}{v_{S_2}} \quad (3-1)$$

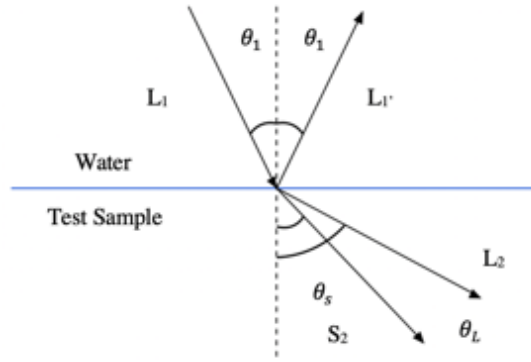


**Figure 12.** Reflection and refraction of acoustic wave at the interface

In general, acoustic waves propagate faster in solids than in fluids, while in one solid medium, longitudinal wave (primary wave) moves faster than shear wave (secondary wave), thus  $v_{L_2} > v_{S_2} > v_{L_1}$ , and  $\theta_L > \theta_s > \theta_1$ .

When the angle of incidence is at the critical angle value, the refracted angle becomes  $90^\circ$ , and the refracted wave propagates along the medium's surface. Specifically, as the incident angle  $\theta_1$  of the longitudinal wave  $L_1$  increase,  $\theta_L$  and  $\theta_s$  will reach  $90^\circ$  in succession, result in two critical angles. When the incident angle slightly exceeds the second critical angle, the Rayleigh wave will be excited at the Rayleigh wave critical angle. Figure 12 illustrates a general relationship between the first critical angle  $\theta_L$ , the second critical angle  $\theta_s$  and the Rayleigh wave critical angle  $\theta_R$ .

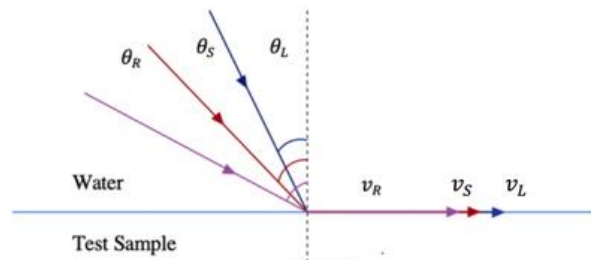


**Figure 13.** A schematic of critical angles for different acoustic waves

### 3.1.2 Detailed measurement principle

A more detailed analysis can be conducted using Figure 13, which shows the lateral schematic of the transducer and the sample at two different positions. This analysis is particularly based on when the surface of the sample is flat. When the upside surface of the sample is placed at the focus plane as Figure 13 (a), all the wave energy that being reflected from the top surface and being received by the transducer travels the same length and thus there are two echo pulses being displayed in the time domain, the first one is the wave directly reflected from the top surface (travel along DOE, BOC, AOA, etc.), and the second one is the wave reflected by the bottom surface of the sample (travel along AFA). As the sample moves toward the transducer by a defocused distance  $z$ , as shown in Figure 13 (b), the Rayleigh wave will be excited. As the Rayleigh wave moving along the surface of the sample, part of the energy will be radiated into the liquid due to the existence of acoustic impedance, in other words, the Rayleigh wave "leaks" into the fluid medium at angle  $\theta_R$ , and such waves are so-called the leaky Rayleigh waves, as shown in Figure 14. Only the leaky surface wave that travels along the incidental wave path and directly radiates towards the lens contributes to the output signal. It is shown by the path DGIHE.

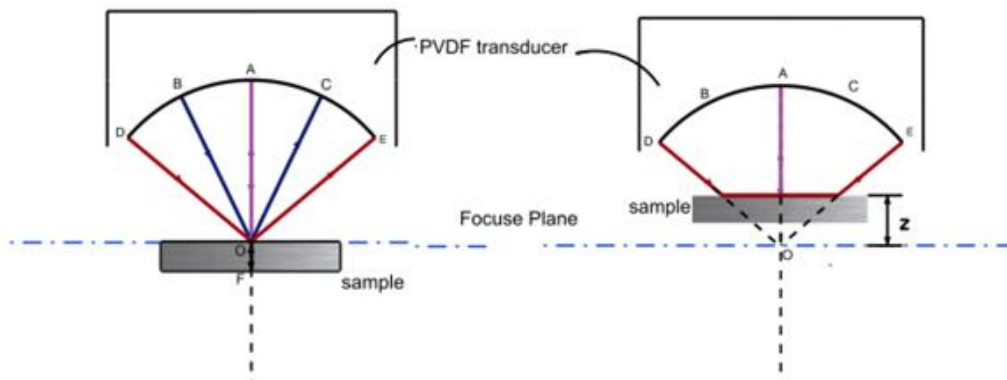


**Figure 14.** The wave propagation of line-focus transducer when (a) sample surface is at the focal plane (b) the sample is defocused with a distance  $z$

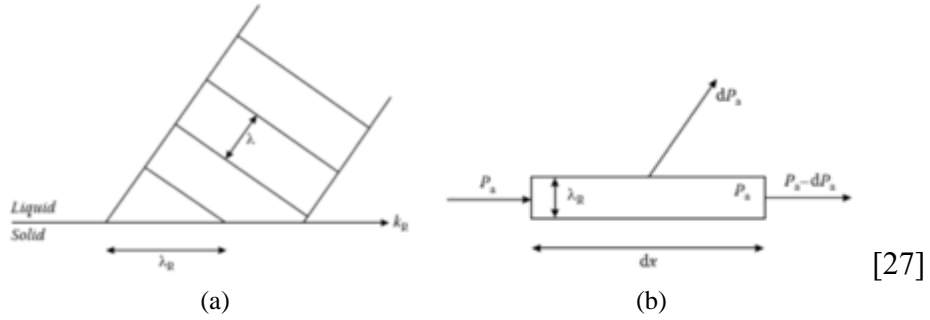


**Figure 15.** a) Radiation of Rayleigh wave from a surface element into an adjacent fluid with acoustic wavelength  $\lambda$   
 (b) Energy balance for a surface element during time  $dt$  due to radiation or leaking of the Rayleigh wave into an adjacent fluid.

Therefore, based on Figure 13 (b), the travel time  $T_1$  of the directly reflected wave could be calculated as:

$$T_1 = \frac{2(R - z)}{v_w} \quad (3-2)$$

where  $R$  is the focal length, and  $v_w$  is the sound velocity in the water. The travel time  $T_2$  of the leaky Rayleigh wave can be calculated as:

$$T_2 = \frac{2(R - \frac{z}{\cos(\theta_R)})}{v_w} + \frac{2z \tan(\theta_R)}{v_R} \quad (3-3)$$

where  $\theta_R$  is the critical angle of Rayleigh waves and  $v_R$  is its velocity. Therefore, the time delay  $dt$  between two main echo pulses is:

$$dt = T_1 - T_2 = \frac{2z \tan(\theta_R)}{v_R} - \frac{2z}{v_w \cos(\theta_R)} + \frac{2z}{v_w} \quad (3-4)$$

According to Snell's law, the relationship between the velocities of sound waves in water and the Rayleigh wave could be represented as:

$$\frac{v_w}{v_R} = \frac{\sin(\theta_R)}{\sin 90^\circ} \quad (3-5)$$

The time delay can then be calculated by applying the Snell's law relationship:

$$dt = \frac{2z}{v_w} (1 - \cos(\theta_R)) \quad (3-6)$$

To further eliminate the  $\theta_R$  items, simplifying Snell's law as:

$$\sin(\theta_R) = \frac{v_w}{v_R} = [1 - (\cos(\theta_R))^2]^{\frac{1}{2}} \quad (3-7)$$

$$\cos(\theta_R) = \left[ 1 - \left( \frac{v_w}{v_R} \right)^2 \right]^{\frac{1}{2}} \quad (3-8)$$

By plugging the  $\cos(\theta_R)$  expression into the simplified time delay formula, the velocity of Rayleigh wave can be represented as:

$$v_R = \left[ \frac{1}{v_w \left( \frac{z}{dt} \right)} - \frac{1}{4 \left( \frac{z}{dt} \right)^2} \right]^{\frac{1}{2}} \quad (3-9)$$

The value of  $\frac{z}{dt}$  can be obtained for each test material through gradually move the transducer towards the specimen by a fixed increment for multiple times. The longitudinal wave velocity inside the specimen can be calculated using the time delay  $\Delta t$  between the front-echo and back-echo surface of the sample, indicating as below equation:

$$v_L = \frac{2d}{\Delta t} \quad (3-10)$$

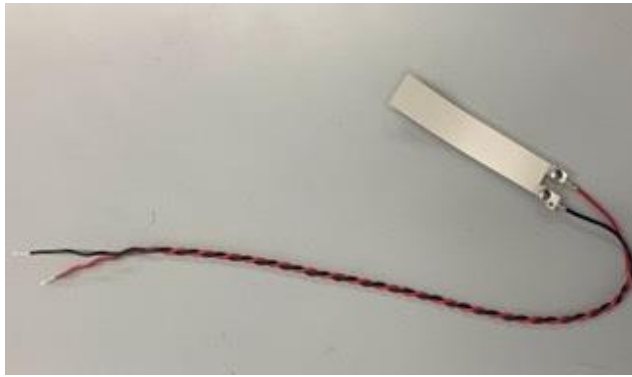
where  $d$  is the thickness of the test sample. After the velocity of Rayleigh wave and longitudinal wave being calculated, the shear wave velocity  $v_S$  can also be calculated using the below equation:

$$\left( \frac{v_S}{v_L} \right)^3 - \left( \frac{v_R}{v_L} \right) \left( \frac{v_S}{v_L} \right)^2 - 0.718 \left( \frac{v_S}{v_L} \right) + 0.75 \left( \frac{v_R}{v_L} \right) = 0 \quad (3-11)$$

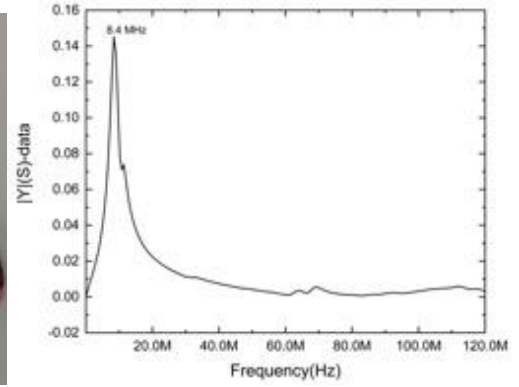
which is derived from the equation that indicates the relationship between the velocity of longitudinal, shear, and Rayleigh wave proposed by Viktorov [18]. Although this formula is of 3<sup>rd</sup> power, resulting in 3 values of  $v_s$  by directly solving it, there is only one solution valid due to the relation that  $v_L > \sqrt{2}v_s$ . After calculating the longitudinal and shear wave velocities, and once the density of the material is measured, the elastic properties can be solved through the formulas in Section 2.2.1.

### 3.2 Transducer Fabrication

The fabrication of this lens-less line focus PVDF transducer refers to the work of Dr. Xiang's team [24]. As mentioned in the theoretic foundation part, to assure the transducer works efficiently, the mechanical parameter of the backing material, the piezoelectric element, and the coupling liquid should be matching. Besides, due to the discard of the front acoustic lens, the piezoelectric element should be flexible enough to attach to the large front curvature of the transducer. The commercial PVDF film, as shown in Figure 15 (a), is selected based on these criteria. Figure 15 (b) shows the test result of its resonance frequency from the impedance analyzer, and it is around 8.4 MHz. The backing material is a mix of tungsten powder and epoxy resin with a weight ratio of 1:2. Figure 16 shows a general procedure for the assembly of the lens-less line-focus transducer.



(a)



(b)

**Figure 16.** (a) PVDF film and (b) its frequency response

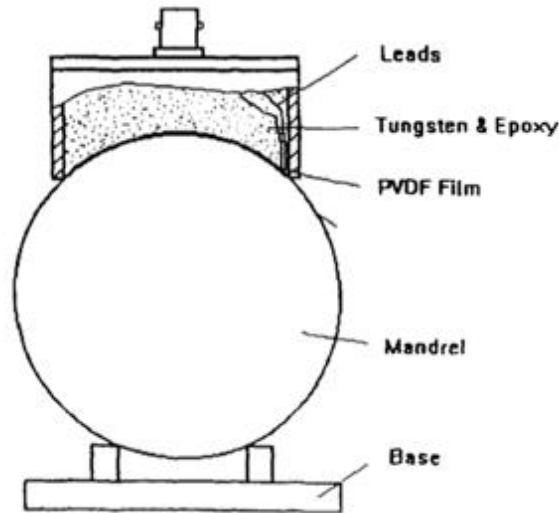


**Figure 17.** The assembly of large aperture lens-less line-focus transducer

An aluminum rectangular tube is machined into a shape with one flat end on the top and one curved end to be later used as the case of the transducer, as shown in Figure 17. The radius of the boundary curve of this machined rectangular tube is consistent with the cylindrical tube, which is used as the mandrel, and its radius is matching with the desired focal length. In our transducer, the focal length is 35mm, and the half aperture angle is 50°.



**Figure 18.** The machined aluminum tube as transducer case.

During the fabrication process, a rectangular tube is firmly placed on the mandrel, while a PVDF film is centered within. Then, casting the mix of tungsten powder and epoxy gel into the rectangular case and waiting until it is fully solidified. The PVDF film will finally be glued with a thin layer of epoxy.

### **3.3 System Configuration**

A schematic of the line-focus ultrasound measurement system was shown as Figure 19. This system's signal processing part includes an ultrasound pulser/receiver (5072PR, OLYMPUS), a digital oscilloscope (4034A, Agilent Technologies), and a line-focus transducer. The pulser/receiver generates the impulse signal and receives the reflected signal from the test sample; the digital oscilloscope can store the data and display the signal; the transducer transmits the signal between electrical and acoustic forms. The mechanical stage controller part, on the other hand, is combined of a motorized stage and a stage controller (DS102, SURUGA SEIKI), which can be controlled through the LabView software on the computer. The line-focus transducer is attached

to the stage controller and fixed by using a screw, as shown in Figure 20. The motorized stage has two-axis control channels available, while in this experiment, only the vertical movement, which alters the distance between the transducer and the specimen, is of interest. The range of stage movement is  $\pm 10\text{mm}$ .

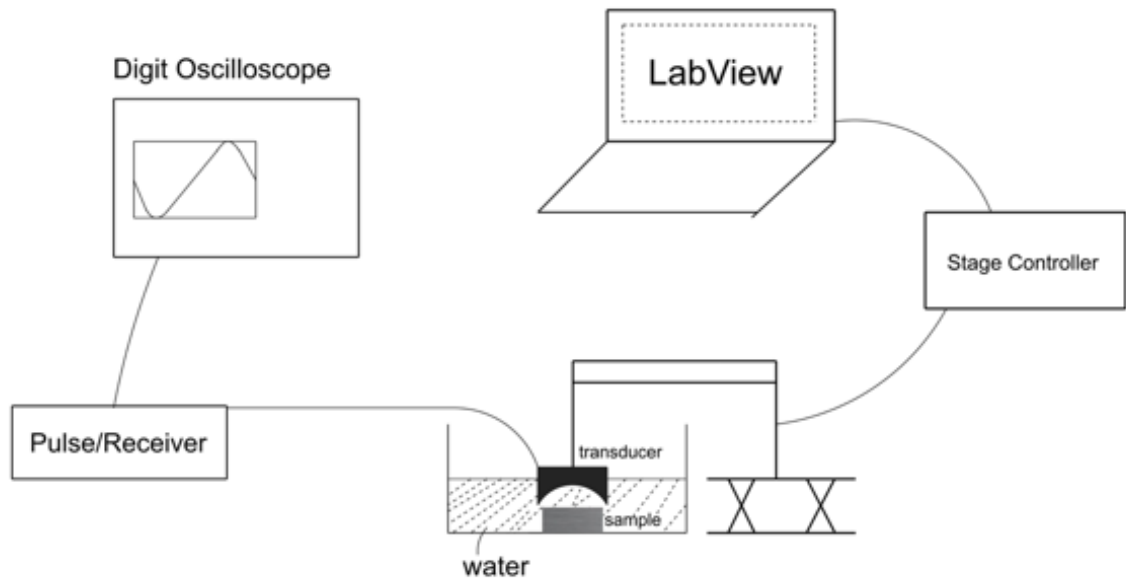


**Figure 19.** A schematic of the measurement system

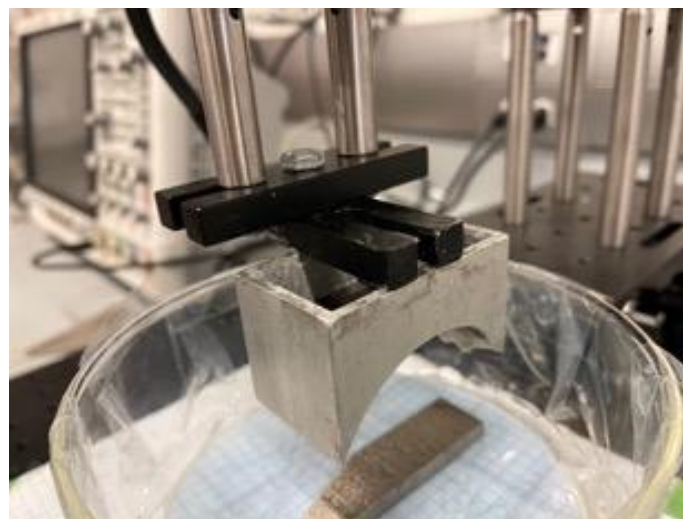
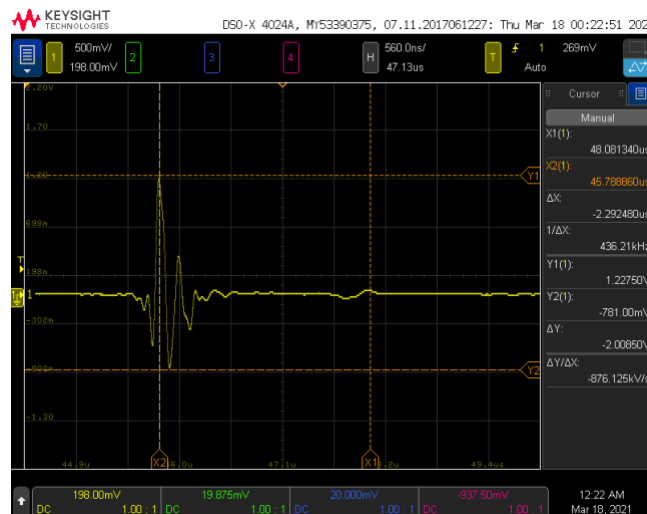
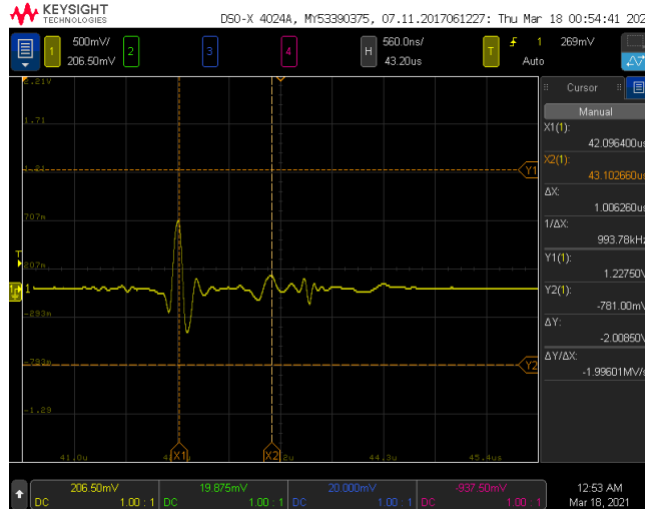


**Figure 20.** The fixation of the transducer to the motor stage

At the beginning of the experiment process, the height of the transducer is adjusted through the stage controller. When the sample's top surface is changed to align with the focal plane, at which the first reflected signal reaches its maximum amplitude while there is no Rayleigh wave reflection received, the measurement starts, and the first set of data is obtained. After that, lower the transducer with a constant step size multiple times and collect the signal data for each position (waveform  $V(t)$  for each defocusing length  $z$ ). Figure 21 (a) shows a sample of the  $V(t)$  curve at the focal position depicted on the oscilloscope, while Figure 21 (b) is an example of the  $V(t)$  curve at defocusing position. During the measurement process, different time delays will be recorded for later calculation. Firstly, since the time delay between the back reflected wave and a directly reflected wave would not change, it was captured once and at the focal position, which is the distance between  $X_1$  and  $X_2$  in Figure 21(a). Secondly, after ten times of defocusing, the time delay between the directly reflected wave and Rayleigh wave of each step was written down, shown as the distance between  $X_1$  and  $X_2$  in Figure 21(b). It should be aware that when capture the time delays using the oscilloscope cursors, the vertical lines have to be placed at the peak point of each wave to minimize gross errors.



(a)



(b)

**Figure 21.** The output signal  $V(t)$  curve when (a) sample surface is at the focal plane (b) the sample is defocused with a distance  $z$

### 3.4 System Calibration

In order to ensure the accuracy of this test method, samples of four common metal alloys, including stainless steel 420, aluminum 6063, and nickel, were used to calibrate the system. During the experiment, the sample placement is carefully aligned with the transducer, and twenty-one sets of data were collected for each sample, starting with one focused point and twenty of the defocusing with a step increment of 0.25mm. Each raw data set contained 2000 points with a  $2E-9$  s time interval. Since the directly reflected wave's travel path decreased as the transducer moved towards the sample, each set of data received the signal in different time intervals. For better visualization and calculation, a MATLAB program is used to align the peak point of the first reflected wave for each data set. A typically aligned wave diagram with appropriate offsets in voltage is shown in Figure 22.

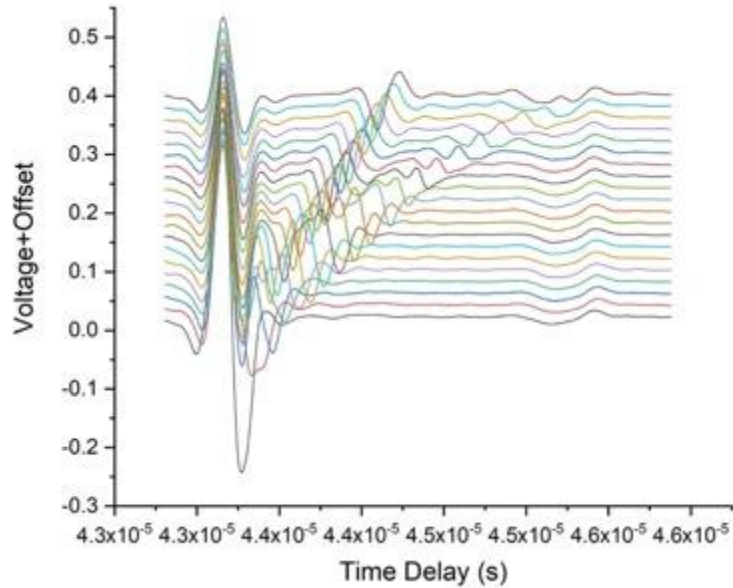


**Figure 22.** Experimental waveform from stainless steel 420 sample

Based on the diagram observation of stainless steel 316 specimen's voltage response in Figure 22, the first peak, denoted as D, is the directly reflected wave from the top surface, while the last peak, denoted as B, is the back reflected wave from the bottom surface. The longitudinal wave velocity can be calculated by the time delay between the front and back reflected waves. Due to the large impedance difference between water and stainless steel, most of the wave energy directly reflected back from the top surface result in a much higher voltage response compared with the other waves. The notation R on Figure 22 represents the Rayleigh wave, and it is obvious that the relationship between the time delay of the Rayleigh wave and the defocused distance  $z$  is almost linear, which complies with the theoretical formula. By extracting the peak data point and making linear interpretation, the Rayleigh wave velocity can be calculated. An example of time delay versus defocused distance diagram is shown in Figure 23. The shear wave velocity can then be solved based on the relationship between the velocity of these three waves. To find the density of the material, a caliper with a  $0.1mm^3$  accuracy was used to calculate the specimen's volume,

while a digital scale with a  $0.0001g$  accuracy was used to measure the mass. With the measured density, longitudinal wave velocity, and shear wave velocity, Young's modulus, shear modulus, and poisson's ratio can be obtained.

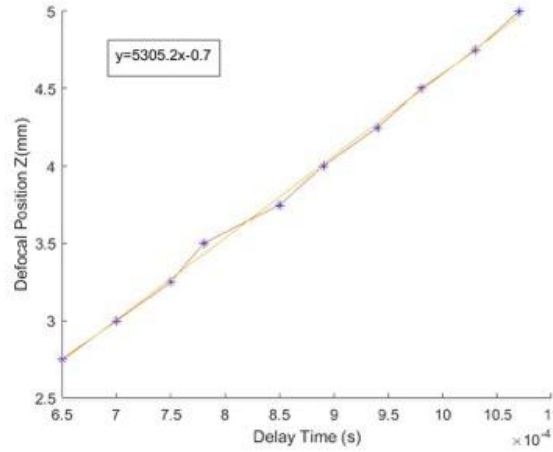


**Figure 23.**  $z(t)$  plot of stainless steel 420

Comparisons of common commercial metal samples' elastic properties between the experimental value and standard value from the ASTM standard are listed in Table 3. The errors between measured density and standard density values are less than 1% for Stainless Steel 420 and Aluminum 6063, while this value for Ni is about 11.2%. As for elastic properties, in terms of SS420, the error between the calculated and standard value of Young's modulus, Shear modulus, and Poisson's ratio are 1.6%, 3.5%, and 4.3%, respectively; for Al 6063, the errors are 0.74%, 1.25%, and 4.8%; for Nickle, these three values are 2.3%, 5.8%, and 10%. Overall, the measured values of elastic properties of commercial alloys have good agreements with standard values, indicating this system to be well-established and accurate.

**Table 3.** Wave velocity and elastic constants of common metal alloys

Material	$v_L$ (m/s)	$v_R$ (m/s)	$v_S$ (m/s)		Density (kg/m <sup>3</sup> )	Young's Modulus (GPa)	Shear Modulus (GPa)	Poisson's Ratio (GPa)
420 SS	5719.3	2905.2	3127.1	Calculated	7.82	196.80	76.47	0.287
				Standard	7.8	200	79.3	0.3
Al 6063	6390.4	2906.1	3098.7	Calculated	2.68	69.52	25.82	0.346
				Standard	2.7	69	25.5	0.33
Ni	5592.3	2891.0	3118.2	Calculated	7.84	194.31	76.24	0.27
				Standard	8.83	190	72	0.30

## 4.0 Experiment Result and Analysis

### 4.1 Additive Manufactured Metals

Three different samples are used in this test, as shown in Figure 24. All of these samples are printed by the EOS M290 (DMLS) machine and made of stainless steel 316L powders, which result in an approximate density of at least  $7.9g/cm$  with standard print parameters. The specific density of each sample was calculated through the mass measured by a digital scale and the volume calculated from the dimensions measured by a caliper. Sample 1 and sample 3 have an approximate density of  $8.11g/cm$ , while sample 2 is  $7.92g/cm$ ; all are very closed to the official data. The components of the raw material are listed in Table 4. Since additive manufacturing produces components layer by layer, although the 3D printed metals are supposed to be isotropic, different orientations of the specimen may exhibit a slight difference in elastic properties. Based on the datasheet listed by EOS, Young's modulus of printed part with standard parameters is about  $185 GPa$  in the horizontal direction (XY) and  $180 GPa$  in the vertical direction (Z). The specimen was aligned carefully with the transducer by using an engineering notebook sheet in order to ensure the consistency of the result, as shown in Figure 24. In this way, the surface wave would propagate along the vertical direction (Z). Also, the surface with the marker of the specimen's number was placed as the bottom surface in order to prevent any unexpected disturbance.

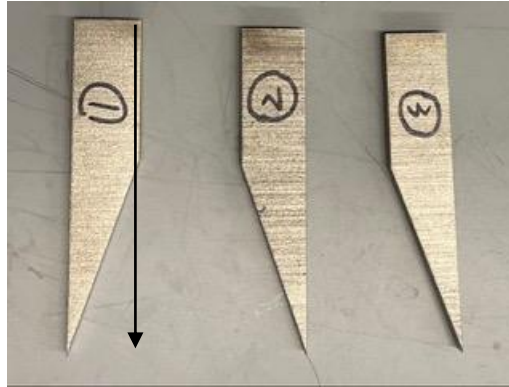


**Figure 24.** 3D printed SS 316L samples with marker

**Table 4.** Material Composition of EOS Stainless Steel 316L

EOS StainlessSteel 316L		
Element	Min	Max
Fe	balance	
Cr	17.00	19.00
Ni	13.00	15.00
Mo	2.25	3.00
C		0.030
Mn		2.00
Cu		0.50
P		0.025
S		0.010
Si		0.75
N		0.10

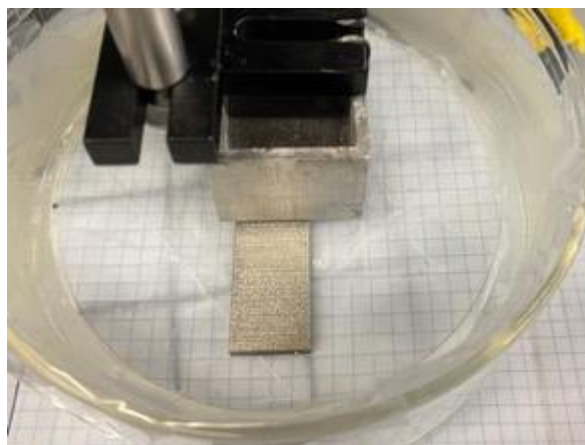


**Figure 25.** Depiction of using engineering notebook sheet to align the sample and transducer

The general test procedure was basically the same as those described in the previous chapters. The transducer would first be adjusted to the focusing position where the direct reflected wave is at the highest amplitude, following by moving downwards to the sample with a fixed increment value. However, for each specimen, two different step size were used other than one, while the total defocusing distance was kept the same as 5mm. In other words, besides the focused point, there are 20 moves when the step size was 0.25mm, and 25 set of data were collected when the step size was 0.2mm. Furthermore sample 1 was measured twice for each step size.

## 4.2 Wave Diagrams and Numerical Result

Based on the above-described testing procedure, eight groups of data in total were collected from these three samples for data analysis. By conducting the same process in the calibration part, each track of testing can generate two diagrams, one is the  $V(z, t)$  wave curves with well-aligned peaks and clear indications of the gradual increasement of Rayleigh wave time delay, while the other one is the  $Z(t)$  plot showing the linear relationship for velocity calculation. Therefore, a total 16 diagrams were obtained and listed as Figure 26 – 41. The MATLAB function *polyfit()* was used to interpret the  $Z(t)$  relationship linearly. Moreover, Table 5 and 6 show all the calculated result, including the velocity of longitudinal, Rayleigh, and shear wave, as well as the elastic properties.

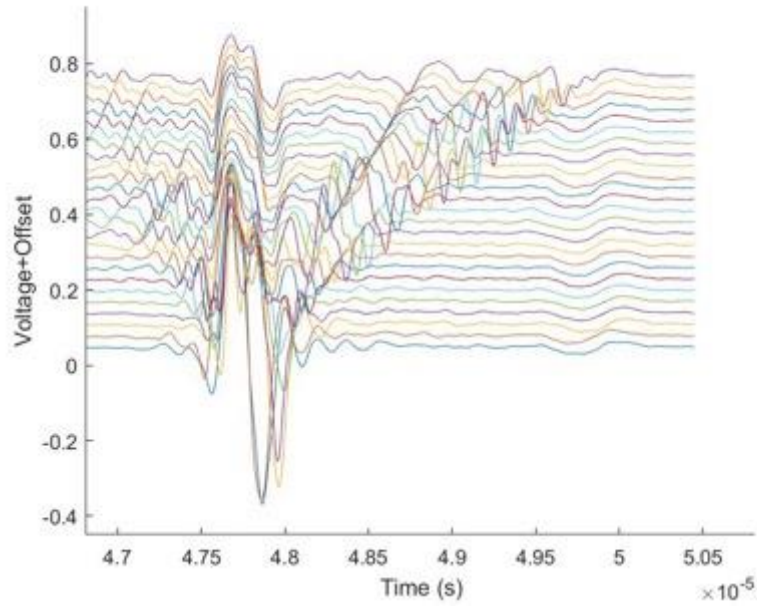


**Figure 26.**  $V(z,t)$  curves of sample 1 with a step size of 0.2, the 1<sup>th</sup> track

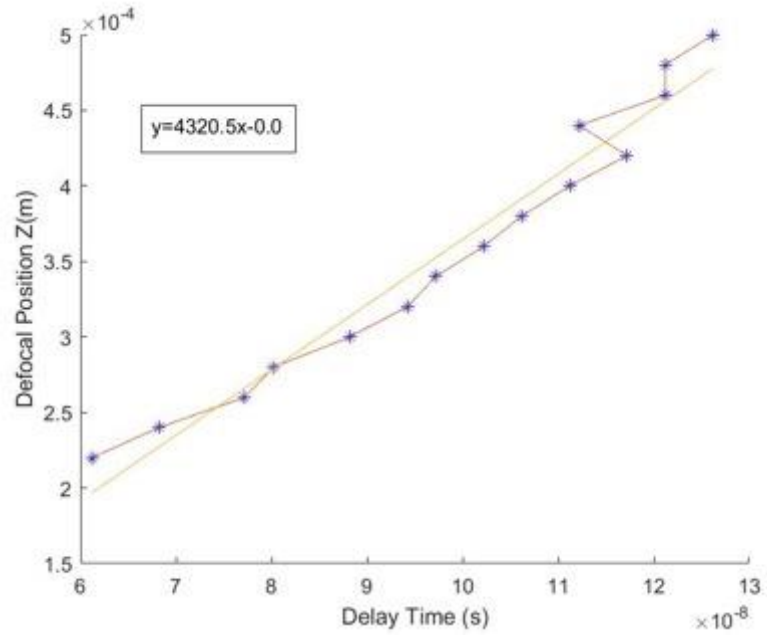


**Figure 27.**  $Z(t)$  plot of sample 1 with a step size of 0.2, the 1<sup>th</sup> track

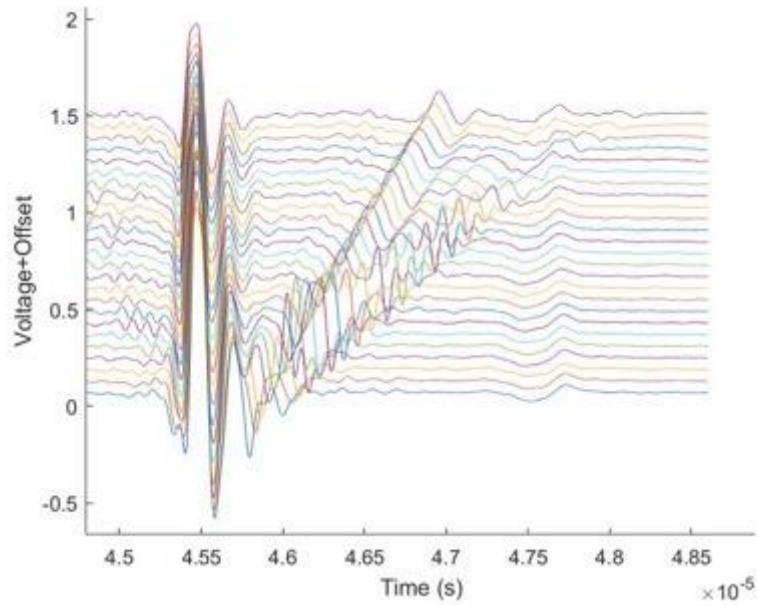


**Figure 28.**  $V(z,t)$  curves of sample 1 with a step size of 0.2, the 2<sup>th</sup> track

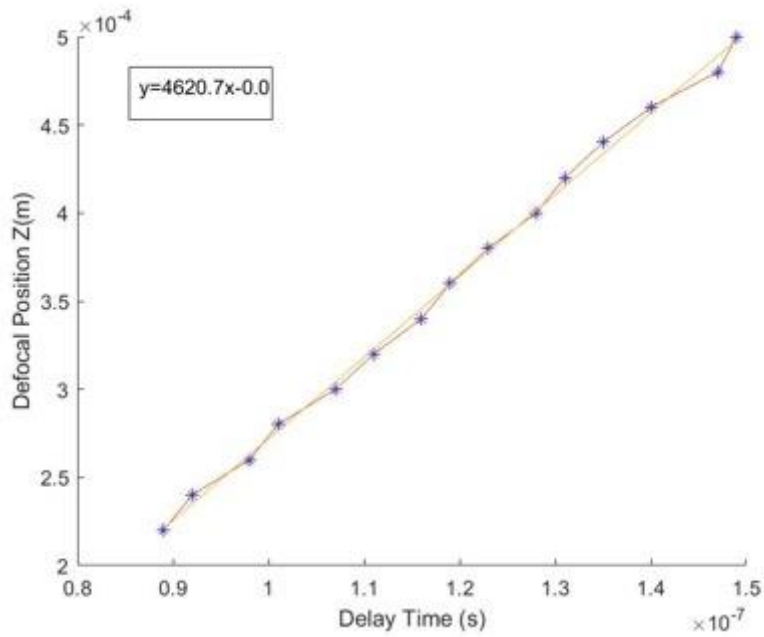


**Figure 29.**  $Z(t)$  plot of sample 1 with a step size of 0.2, the 2<sup>th</sup> track

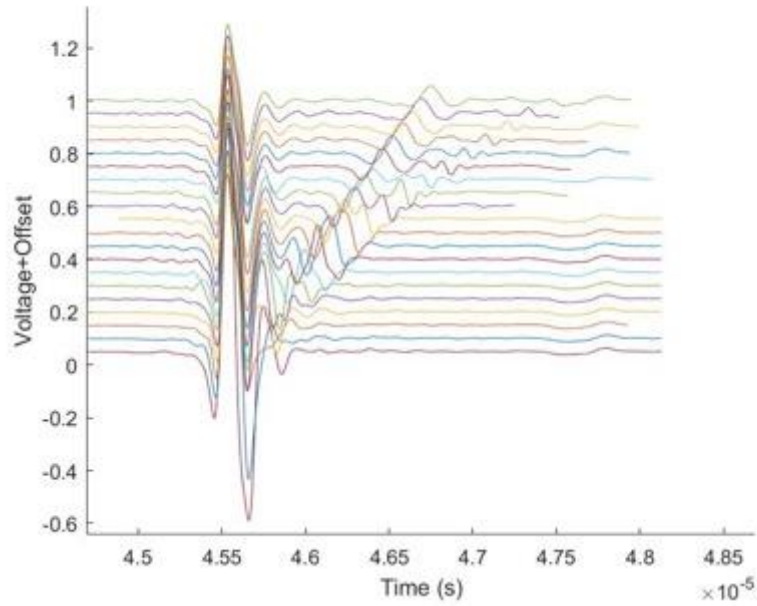


Figure 30.  $V(z,t)$  curves of sample 1 with a step size of 0.25, the 1<sup>th</sup> track

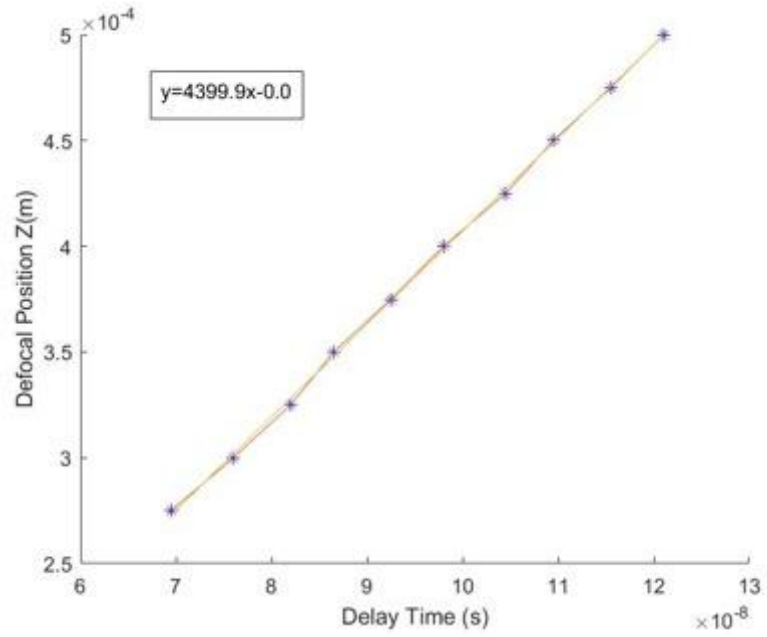
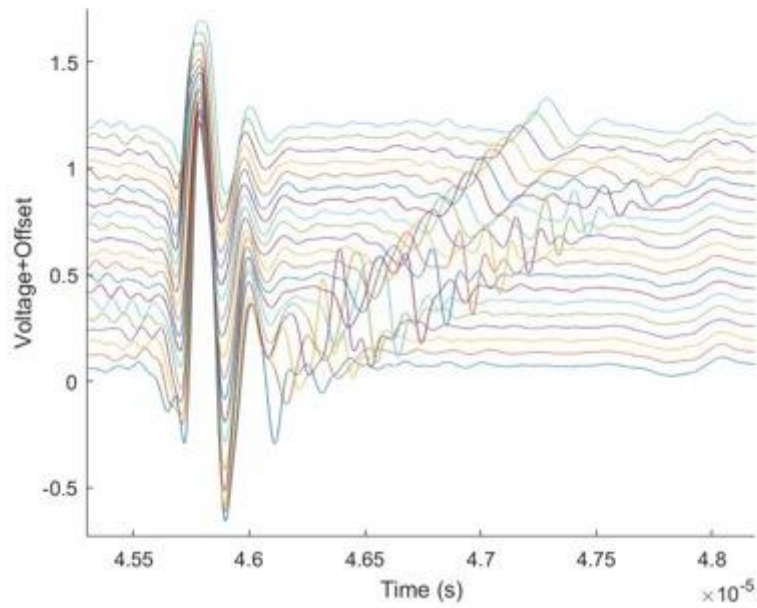
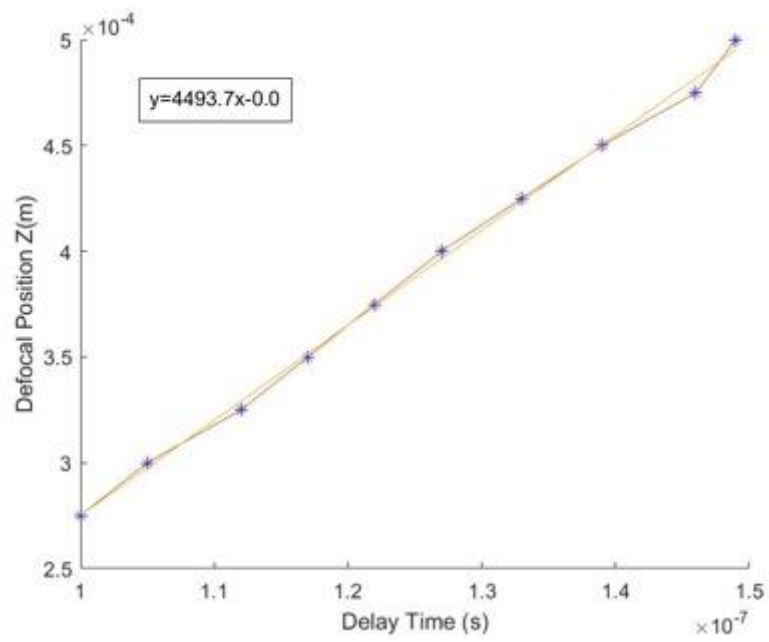


Figure 31.  $Z(t)$  plot of sample 1 with a step size of 0.25, the 1<sup>th</sup> track



**Figure 32.**  $V(z,t)$  curves of sample 1 with a step size of 0.25, the 2<sup>th</sup> track



**Figure 33.**  $Z(t)$  plot of sample 1 with a step size of 0.25, the 2<sup>th</sup> track

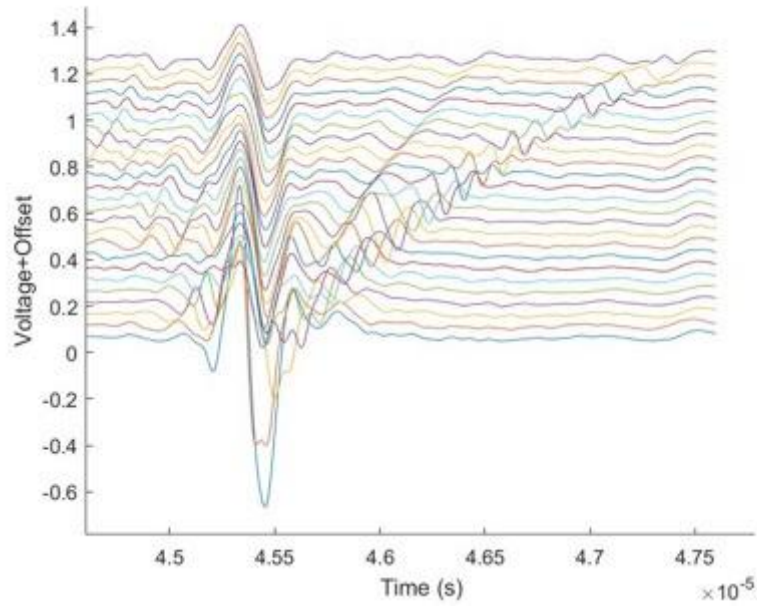


**Figure 34.**  $V(z,t)$  curves of sample 2 with a step size of 0.2

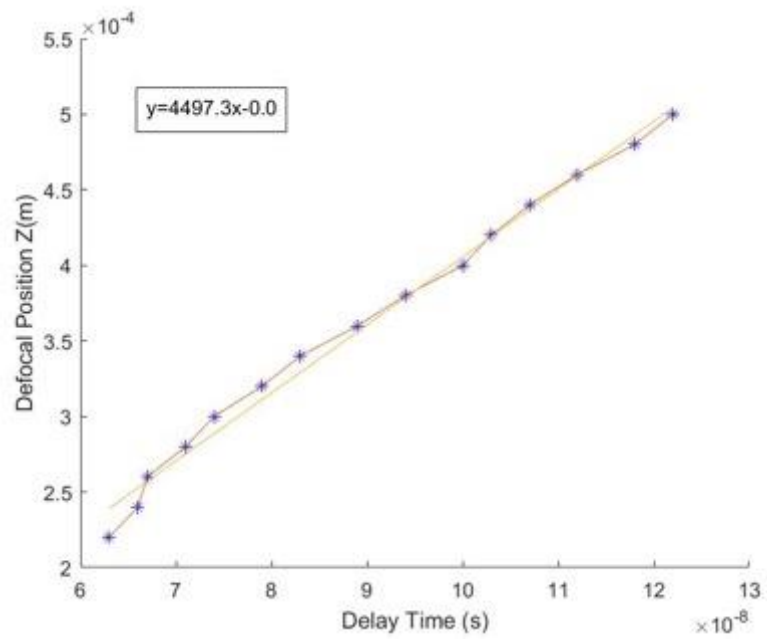


**Figure 35.**  $Z(t)$  plot of sample 2 with a step size of 0.2

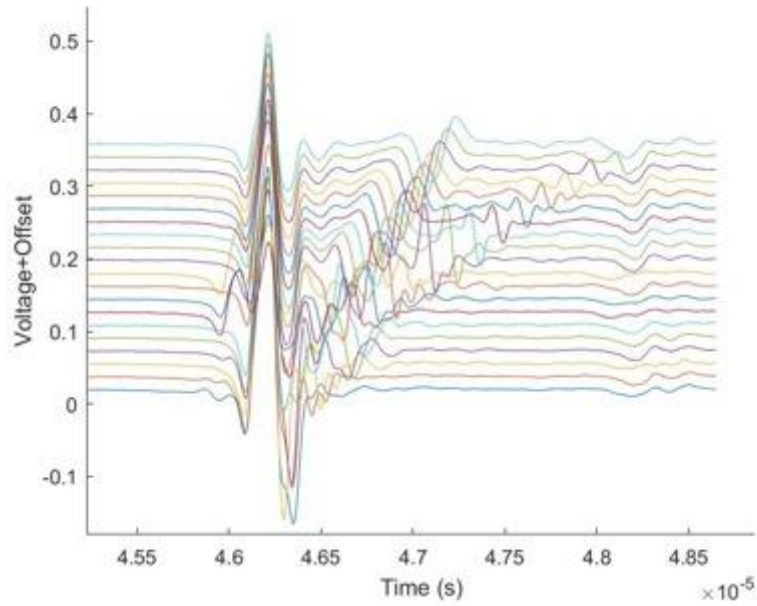


**Figure 36.**  $V(z,t)$  curves of sample 2 with a step size of 0.25

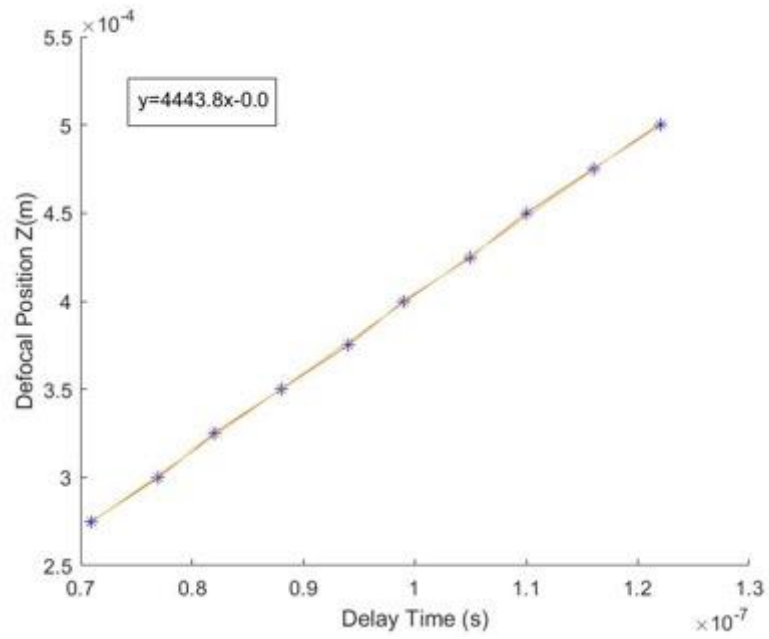


**Figure 37.**  $Z(t)$  plot of sample 2 with a step size of 0.25

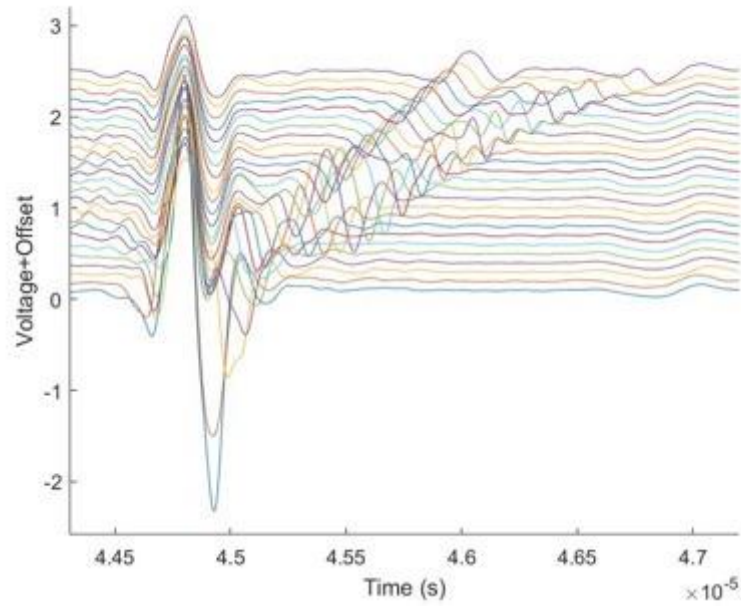


**Figure 38.**  $V(z,t)$  curves of sample 3 with a step size of 0.2

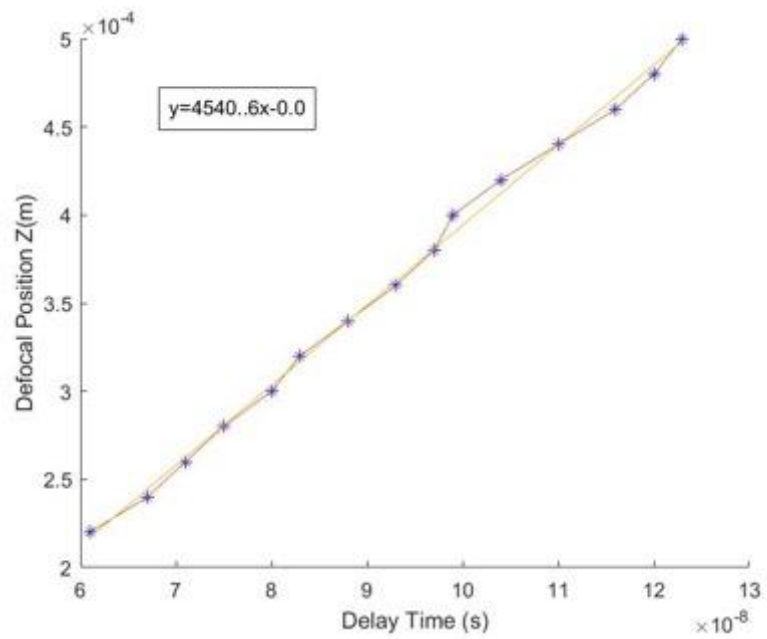


**Figure 39.**  $Z(t)$  plot of sample 3 with a step size of 0.2

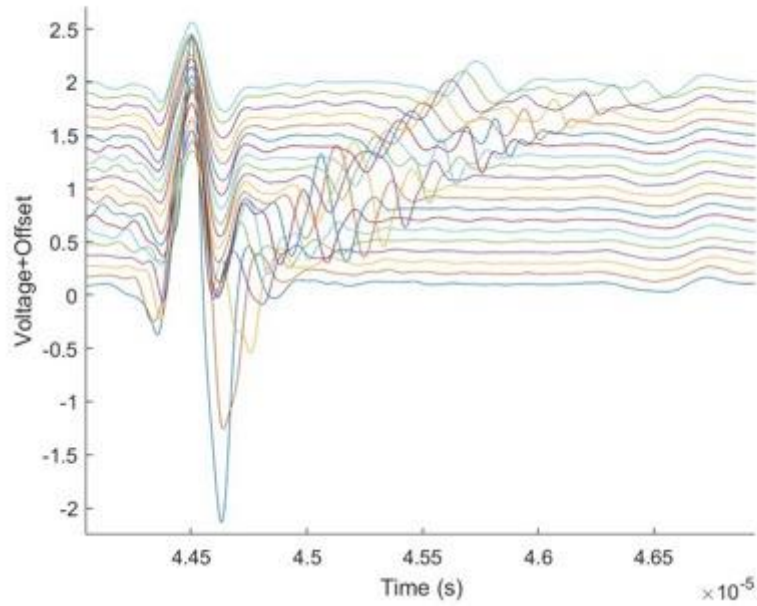


**Figure 40.**  $V(z,t)$  curves of sample 3 with a step size of 0.25

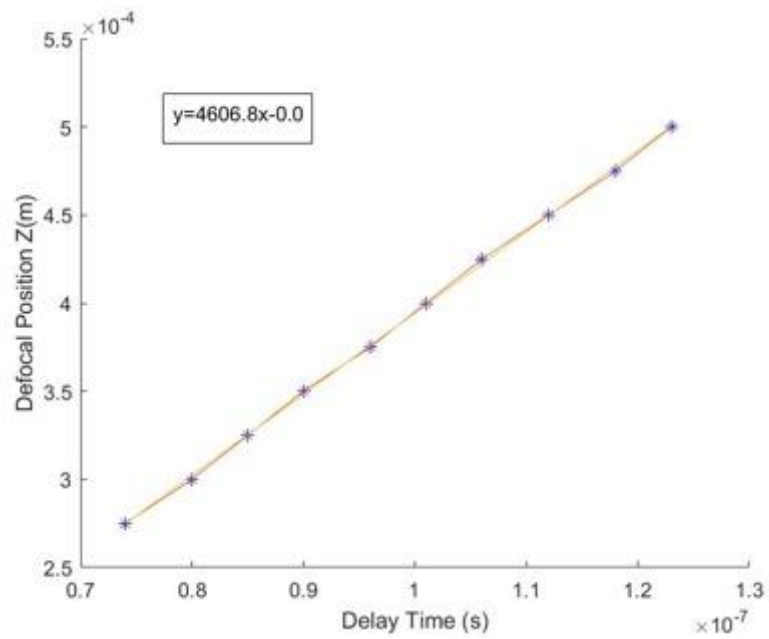


**Figure 41.**  $Z(t)$  plot of sample 3 with with a step size of 0.25

**Table 5.** Calculated result of sample 1

	<i>Sample 1</i>			
<i>Step Size (mm)</i>	0.2		0.25	
<i>Track #</i>	Track 1	Track 2	Track 1	Track 2
<i>Density</i>	8.11	8.11	8.11	8.11
<i>Slope</i>	4320.5	4620.7	4399.9	4493.7
$v_L$ (m/s)	5251.1	5272	5191.6	5252.5
$v_R$ (m/s)	2644.5	2726.5	2666.4	2692.1
$v_S$ (m/s)	2843.7	2941	2873.7	2900.7
<i>Young's Modulus (GPa)</i>	169.6	178.8	171.4	174.8
<i>Shear Modulus (GPa)</i>	65.6	70.2	67	68.3
<i>Poisson's Ratio</i>	0.292	0.274	0.279	0.281

**Table 6.** Calculated result of sample 2 and sample 3

	<i>Sample 2</i>		<i>Sample3</i>	
<i>Stap Size (mm)</i>	0.2	0.25	0.2	0.25
<i>Density(m/s)</i>	7.92	7.92	8.11	8.11
<i>Slope</i>	4497.3	4443.8	4540.6	4606.8
$v_L$ (m/s)	5643.3	5252.5	5297.9	5375.3
$v_R$ (m/s)	2693.1	2678.5	2704.9	2722.8
$v_S$ (m/s)	2881.5	2884.3	2913.1	2929.7
<i>Young's Modulus (GPa)</i>	174	169.1	176.7	179.5
<i>Shear Modulus (GPa)</i>	65.7	65.9	68.8	69.6
<i>Poisson's Ratio</i>	0.324	0.284	0.283	0.289

In general, there is no significant fluctuation of results appears within these 8 tracks of testing. According to the numbers listed in Table 5, the average value of measured Young's modulus, Shear Modulus and Poisson's ratio of sample 1 are 173.65 *GPa*, 67.76 *GPa*, and 0.28 with a relative standard deviation of 2.33%, 2.89%, and 2.70%, respectively, showing a good consistency that verifies the precision of this method. By analyzing all three samples' data listed in both Table 5 and 6, the overall average result of elastic properties among all the samples are 174.43 *GPa* (Young's modulus), 67.59 *GPa* (Shear Modulus), and 0.29 (Poisson's ratio) with a relative standard deviation of 1.9%, 2.5%, and 4.09%. Figure 42 – 43 show the averaging value of calculated elastic properties with standard deviation error bars. Within each figure, the left point indicates the result of sample 1 from four different testing tracks, while the right point represents the overall result of three samples. Compared the measured sample mean to the standard Young's

modulus value from the datasheet as 180 *GPa*, the error is around 3.09%. Additionally, by looking up corresponding t-scores of 95% confidence interval and computing the standard error, a rough prediction of the actual elastic properties based on the test result can be calculated, as shown in Table 7.



**Figure 42.** The average Young's modulus with standard deviation error bar

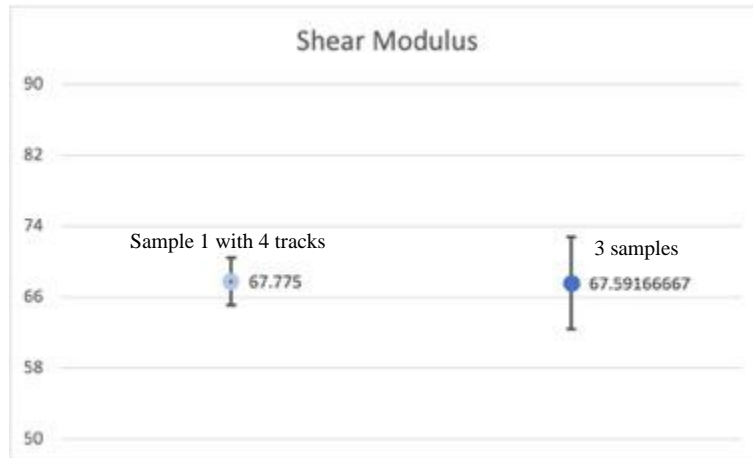


**Figure 43.** The average shear modulus with standard deviation error bar

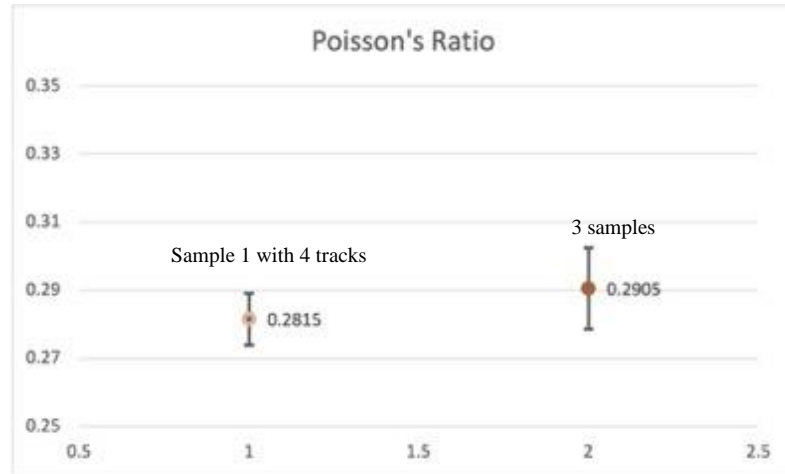


**Figure 44.** The average Poisson's ratio with standard deviation error bar

**Table 7.** A predicted range of actual elastic properties based on testing results

	<i>Sample 1</i>	<i>3D printed SS316L bar</i>
<i>Young's Modulus (GPa)</i>	[168.1, 179.2]	[164.3, 184.6]
<i>Shear Modulus (GPa)</i>	[65.1, 70.43]	[62.3, 72.8]
<i>Poisson's Ratio</i>	[0.27, 0.29]	[0.25, 0.33]

### 4.3 Summary

As stated by the data in the previous section, the results have good repeatability with reasonable discrepancies, and the averaging Young's modulus value of these three samples is close to the official number. By conducting statistical analysis, the actual value interval could be predicted when the data have multiple groups. Since the number of experiments and samples was not large enough, more test tracks could be designed in the future to shrink the value range, and the result will be more accurate. Consider the Rayleigh wave propagating on the above surface of

the samples and the special features of 3D printing, the roughness of the sample should be taken into account. According to the official datasheet, the roughness of printed metals without surface finishing would be around  $R_a = [5, 20] \mu m$ . The average Rayleigh wave velocity from the measurement is around  $2691.1 m/s$ , and the central frequency of the transducer is about  $8.4 MHz$ . Thus, the wavelength can be calculated as around  $\lambda = \frac{v}{f} = 320.4 \mu m$ . Since the wavelength is more than ten times of the roughness,  $R_a$  should not affect the accuracy of this method much. Another noticeable factor that could impact the test result is from Rayleigh wave time delay recording. Sometimes the received wave will deform due to unknown reasons, as what is shown in Figure 26. Although the oscilloscope settings are always adjusted to reach a better observation of the wave, the time delays are hard to precisely captured due to the indistinct peak on some occasions, and this could result in some unwanted errors.

## 5.0 Future Work

The line-focus transducer system presented in this research provided the explicit value of the elastic properties of measured samples. The system is highly controlled, cost-effective, and easy to set up and operated. The experiment procedure is clear and time-efficient, while the subsequent data analysis is tidy and well-designed. This system and measurement theory could be widely used in pertinent areas. Future improvement could be carried on the transducer modification. Firstly, the transducer dimension could be tailored to accommodate different conditions, as long as the incident angle could reach the Rayleigh wave critical angle. The 3D printing technology could also be considered using in transducer outer tube fabrication if different sizes of the transducer are needed, and the conventional manufacturing is relatively inconvenient. Additionally, the measurement principle in this thesis was only derived for samples with a flat surface, limiting the applications to a certain extent. For example, currently derived relationships could not be applied if the specimen is a cylinder metal bar as shown in Figure 45, despite the linearly time delay increasing exist according to Song's work, as shown in Figure 46 and 47 [28].



**Figure 45.** A 3D printed cylinder metal bar

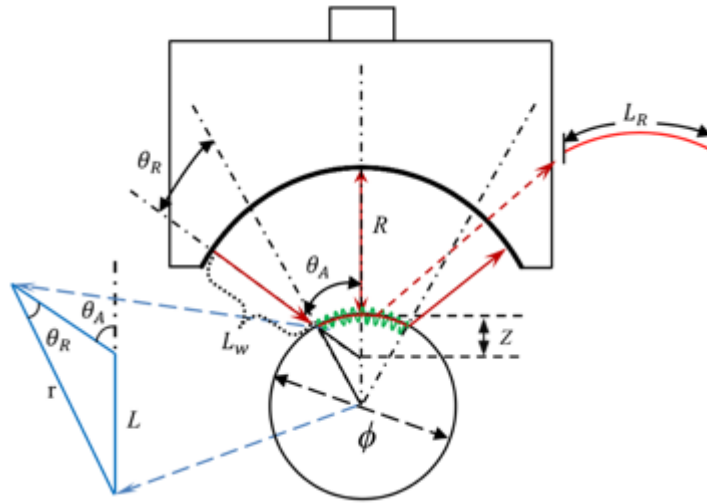


**Figure 46.** Schematic of line-focus transducer measurement principle with a cylinder sample

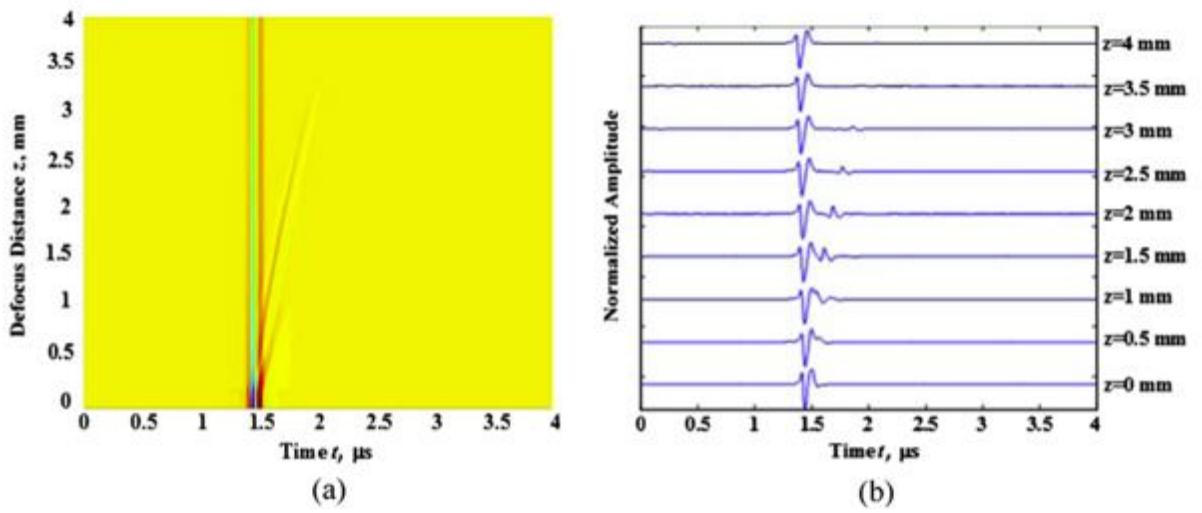


**Figure 47.** (a) measured waveforms of 3D-time domain; (b) normalized waveforms of time domain

## Appendix A MATLAB Program

(1) MATLAB code for acquiring plot and find longitudinal wave velocity

```
clear;clc
%%The first part is to determine the intrinsic property of
the material
M=68.0292;%mass in g
V=8.3844;%volume in ml
density=M/V*1000 %density in kg/m3
%The thickness is used for calculate longitudinal bulk wave
d=5.96; %thickness in mm
Defocus_Time=xlsread('Linear_Interpolation_3D_Printing_3');
figure(1);
RealTime=Defocus_Time(:,3)/(10e9)
RealDe=Defocus_Time(:,2)/(10e3)
scatter(RealTime,RealDe,'b','*');
hold on
plot(RealTime,RealDe);
%title('Z(t) Plot 3D Printing');
xlabel('Delay Time (s)');
ylabel('Defocal Position Z(m)');
P = polyfit(RealTime,RealDe,1)
format long
plot(RealTime,P(1)*RealTime+P(2))
format short
slope=P(1)

%%import the data of focus point
Focus=csvread('focus1.csv',2,0);
%%Plot the diagram of the focus point
figure(2);
%plot(Focus(:,1),Focus(:,2));
%title('Curves of Rayleigh Wave Propagation 3D Printing');
xlabel('Time (s)');
ylabel('Voltage+Offset');
hold on
%Find the highest reflection (Longitudinal Wave)
[value,position]=max(Focus(:,2));
x_value=Focus(:,1);
Highest_time=x_value(position,1);
%Find the longitudinal bulk wave reflection
%The Time Delay was calculated from the values of the focus
point
```

```

    %The time delay is the time between the highest point of the
first
    %reflection wave and the longitudinal bulk wave
    Back_Reflect_x=Focus(:,1);
    Back_Reflect_y=Focus(:,2);
    Find_Back=[0,0];
    for j=1:length(Back_Reflect_x(:,1))
        if Back_Reflect_x(j)>4.969e-5 &&
Back_Reflect_x(j)<4.995e-5
            Find_Back=[Find_Back;Back_Reflect_x(j),Back_Reflect_y(j)];
        end
    end
    [Bulk_Value,Bulk_Position]=max(Find_Back(:,2));
    Bulk_Time=Find_Back(Bulk_Position,1);
    TimeDelay_BulkWave=Bulk_Time-Highest_time;
    V_L=2*d/1000/TimeDelay_BulkWave
    Aligned_Data=[];
for i=1:10
    j=num2str(i);
    filename=['scope0',j];
    filename1=[filename, '.csv'];
    Data=csvread(filename1,2,0);%Import each data set from 1-
10
    %set the offset of y (with increment of 0.1)
    a=Data(:,2);
    b=length(a);
    offset=0.03*i*ones(b,1);
    Data(:,2)=Data(:,2)+offset;
    %Align the highest point (find the offset of x-axes)
    [value1,position1]=max(Data(:,2));
    x_value1=Data(:,1);
    offset_x=Highest_time-x_value1(position1,1);
    offset_x=offset_x*ones(b,1);
    Data(:,1)=Data(:,1)+offset_x;
    Time=Data(:,1);
    Count=1;
    CountNeed=1;
    DataNeed=[];
    while Count <=length(Time)
        if Time(Count)>=4.68e-5 && Time(Count)<=5.045e-5;
            DataNeed(CountNeed,1:2)=Data(Count,:);
            CountNeed=CountNeed+1;
        end
        Count=Count+1;
    end
    plot(DataNeed(:,1),DataNeed(:,2));

```

```

    hold on
    %Alighed_Data=[Alighed_Data Data];
end
for i=1:15
    k=num2str(i);
    filename=['step',k];
    filename1=[filename, '.csv'];
    Data=csvread(filename1,2,0); %Import each data set from 1-
10
    %set the offset of y (with increment of 0.1)
    a=Data(:,2);
    b=length(a);
    offset=0.03*(i+10)*ones(b,1);
    Data(:,2)=Data(:,2)+offset;
    %Align the highest point (find the offset of x-axes)
    [value1,position1]=max(Data(1:800,2));
    x_value1=Data(:,1);
    offset_x=Highest_time-x_value1(position1,1);
    offset_x=offset_x*ones(b,1);
    Data(:,1)=Data(:,1)+offset_x;
    Time=Data(:,1);
    Count=1;
    CountNeed=1;
    DataNeed=[];
    while Count <=length(Time)
        if Time(Count)>=4.68e-5 && Time(Count)<=5.045e-5;
            DataNeed(CountNeed,1:2)=Data(Count,:);
            CountNeed=CountNeed+1;
        end
        Count=Count+1;
    end
    plot(DataNeed(:,1),DataNeed(:,2));
    hold on
    %plot(Data(:,1),Data(:,2));
    %Alighed_Data=[Alighed_Data Data];
end

```

## (2) MATLAB code for computing elastic properties

```

%slope=z/dt;
%This is what we can get from the experiment
%Surface Wave
V_W=1480;
%Rayleigh surface wave velocity
V_R=(1/(V_W*slope)-1/4/(slope^2))^-0.5;
%longitudinal bulk wave velocity,get from the experiment as
well

```

```

V_L;
syms V_T;
tho=density;
[V_T]=solve((V_T/V_L)^3-(V_R/V_L)*((V_T/V_L)^2)-
0.718*(V_T/V_L)+0.75*(V_R/V_L)==0);
V_T=double(V_T);
V_T=abs(V_T);
L=length(V_T);
for i=1:L
    if V_T(i)< (V_L/(2^0.5))
        answer=V_T(i);
    end
end
V_T=answer;
C_L=V_L
C_R=V_R
C_S=V_T
%density unit is kg/m^3
E=(tho*(V_T)^2*(3*(V_L^2)-4*(V_T^2))/(V_L^2-
V_T^2))/(10^9)%The Young's Modulus
G=(tho*V_T^2)/(10^9)%The Shear modulus
v=(2*V_T^2-V_L^2)/(2*(V_T^2-V_L^2))%Poisson's ratio

```

## Bibliography

- [1] K. Uchino, *Advanced Piezoelectric Materials - Science and Technology* (2nd Edition), Woodhead Publishing, 2017.
- [2] Q. Qin, *Advanced Mechanics of Piezoelectricity*, Berlin, Heidelberg: Springer, 2013.
- [3] W. Heywang, K. Lubitz and W. Wersing, *Piezoelectricity: Evolution and Future of a Technology*, Springer, 2008.
- [4] K. Uchino, *Advanced Piezoelectric Materials - Science and Technology*, Woodhead Publishing, 2010.
- [5] M. S. Vijaya, *Piezoelectric Materials and Devices : Applications in Engineering and Medical Sciences*, Boca Raton, FL: Taylor & Francis Group, 2013.
- [6] Y. Hu, W. Kang, Y. Fang, L. Xie, L. Qiu and T. Jin, "Piezoelectric Poly(vinylidene fluoride) (PVDF) Polymer-Based Sensor for Wrist Motion Signal Detection," *Applied Science*, vol. 8, no. 836, 2018.
- [7] APC International, Ltd., "MODES OF VIBRATION FOR PIEZOELECTRIC ELEMENTS," APC International, Ltd., [Online]. Available: <https://www.americanpiezo.com/knowledge-center/piezo-theory/vibration.html>.
- [8] A. Pye, "prospector," prospector., 30 June 2015. [Online]. Available: <https://knowledge.ulprospector.com/2689/pe-piezoelectric-materials/>. [Accessed 23 2021].
- [9] W. Contributors, "Destructive testing," Wikipedia, The Free Encyclopedia, 31 January 2021. [Online]. Available: [https://en.wikipedia.org/w/index.php?title=Destructive\\_testing&oldid=1003955022](https://en.wikipedia.org/w/index.php?title=Destructive_testing&oldid=1003955022). [Accessed 2 March 2021].
- [10] M. S. Xavier, S. Yang, C. Comte, A. Bab-Hadiasher, N. Wilson and I. Cole, "Nondestructive quantitative characterization of material phases in metal additive manufacturing using multi-energy synchrotron X-rays microtomography," *The International Journal of Advanced Manufacturing Technology*, no. 106, pp. 1601-1615, 2020.
- [11] "Basic Principles of Ultrasonic Testing," NDT Resource Center, [Online]. Available: <https://www.nde-ed.org/EducationResources/CommunityCollege/Ultrasonics/Introduction/description.htm>.
- [12] H. Tetsuka and S. R. Shin, "Materials and technical innovations in 3D printing in biomedical applications," *Journal of Materials Chemistry*, vol. B, pp. 2930-2950, 2020.
- [13] E. E. Boudouti, B. Djafari-Rouhani, A. Akjouj, and L. Dobrzynski, "Acoustic waves in solids and fluid, layered materials," *Surface Science Reports*.
- [14] D. S. J. Ballantine, R. M. White, S. J. Martin, A. J. Ricco, G. C. Frye, E. T. Zellars and H. Wohltjen, *Acoustic Wave Sensors - Theory, Design and Physico-Chemical Applications*, Elsevier, 2007.

- [15] MIT AEROASTRO, "Structural Mechanics," MIT AEROASTRO, 2013. [Online]. Available: [http://web.mit.edu/16.20/homepage/CourseInfo/CourseInfo\\_files/course\\_information.pdf](http://web.mit.edu/16.20/homepage/CourseInfo/CourseInfo_files/course_information.pdf). [Accessed 3 3 2021].
- [16] J. D. N. Cheeke, *Fundamentals and Applications of Ultrasonic Waves*, Taylor&Francis Groups, 2012.
- [17] T. Kundu, *Mechanics of Elastic Waves and Ultrasonic Nondestructive Evaluation*, Taylor & Francis Group, 2019.
- [18] Q. Li, X. Zhang, Y. Wang and W. Qing-Ming, "CHARACTERIZATION OF MATERIALS FABRICATED BY ADDITIVE MANUFACTURING METHOD USING LINE FOCUSED ULTRASONIC TRANSDUCER," in *2016 International Mechanical Engineering Congress & Exposition*, Phoenix, 2016.
- [19] R. Lemons and C. Quate, "Acoustic microscope—scanning version," *Applied Physics Letters*, no. 24, pp. 163-165, 1974.
- [20] J.-I. KUSHIBIKI and N. CHUBACHI, "Material Characterization by Line-Focus-Beam Acoustic Microscope," *IEEE TRANSACTIONS ON SONICS AND ULTRASONICS*, Vols. SU-32, no. 2, pp. 189-212, 1985.
- [21] w. Parmon and H. Bertoni, "Ray Interpretation of the Material Signature in the Acoustic Microscope," *Electronics Letters*, vol. 15, no. 21, pp. 684-686, 1979.
- [22] "Surface acoustic wave measurements using an impulsive converging beam," *Journal of Applied Physics*, vol. 54, no. 8, pp. 4323-4329, 1983.
- [23] K. Liang, S. D. Bennett, B. T. Khuri-Yakub and G. S. Kino, "Surface Wave Velocity Measurements at 50 Megahearts," in *IEEE ULTRASONIC SYMPOSIUM*, Stanford, 1982.
- [24] D. Xiang, N. Hsu and G. Blessing, "The design, construction and application of a large aperture lens-less line-focus PVDF transducer," *Ultrasonics*, vol. 34, no. 6, pp. 641-647, 1996.
- [25] N. N. Hsu, S. E. Fick, Blessing, and G. V., "GREEN'S FUNCTION OF A LIQUID/SOLID INTERFACE AND APPLICATION TO FLUID COUPLED ULTRASONIC MATERIALS TESTING," in *IEEE ULTRASONICS SYMPOSIUM*, 1992.
- [26] N. N. Hsu, D. Xiang, S. E. Fick, and G. V. Blessing, "TIME AND POLARIZATION RESOLVED ULTRASONIC MEASUREMENTS USING A LENSLESS LINE-FOCUS TRANSDUCER," in *IEEE ULTRASONICS SYMPOSIUM*, 1995.
- [27] J. David and N. Cheeke, *Fundamentals and Applications of Ultrasonic Waves*, Boca Raton: Taylor & Francis Group, 2012.
- [28] G. Song, D. Lu, Y. Lu, H. Liu, Z. Gao, B. Wu and C. He, "Velocity measurements of cylindrical surface waves with a large aperture line-focus acoustic transducer," *Measurement*, vol. 90, pp. 103-109, 2016.